A Nonhydrostatic Multiscale Model on the Uniform Jacobian Cubed Sphere

MIODRAG RANČIĆ, R. JAMES PURSER, DUŠAN JOVIĆ, AND RATKO VASIC

I. M. Systems Group, Inc., NOAA/NCEP/Environmental Modeling Center, College Park, Maryland

THOMAS BLACK

NOAA/NCEP/Environmental Modeling Center, College Park, Maryland

(Manuscript received 11 May 2016, in final form 21 November 2016)

ABSTRACT

The rapid expansion of contemporary computers is expected to enable operational integrations of global models of the atmosphere at resolutions close to 1 km, using tens of thousands of processors in the foreseeable future. Consequently, the algorithmic approach to global modeling of the atmosphere will need to change in order to better adjust to the new computing environment. One simple and convenient solution is to use low-order finite-differencing models, which generally require only local exchange of messages between processing elements, and thus are more compatible with the new computing environment. These models have already been tested with physics and are well established at high resolutions over regional domains. A global nonhydrostatic model, the Nonhydrostatic Multiscale Model on the B grid (NMMB), developed at the Environmental Modeling Center of the National Centers for Environmental Prediction during the first decade of this century is one such model. A drawback of the original version of global NMMB is that it is discretized on the standard longitude–latitude grid and requires application of Fourier polar filtering, which is relatively inefficient on massively parallel computers. This paper describes a reformulation of the NMMB on the grid geometry of a novel cubed sphere featuring a uniform Jacobian of the horizontal mapping, which provides a uniform resolution close to that of the equiangular gnomonic cubed sphere, but with a smooth transition of coordinates across the edges. The modeling approach and encountered challenges are discussed and several results are shown that demonstrate the viability of the approach.

1. Introduction

This paper describes a cubed-sphere version of a global, nonhydrostatic model of the atmosphere, the Nonhydrostatic Multiscale Model on the B grid (NMMB) (e.g., Janjić et al. 2001; Janjić 2003; Janjić and Gall 2012), developed at the Environmental Modeling Center (EMC) of the National Centers for Environmental Prediction (NCEP). The NMMB was developed in both regional and global modes, the latter using the standard longitude–latitude (or geographical) grid, with polar filtering of Arakawa and Lamb (1977) as a technique to deal with the linear stability restrictions imposed by the convergence of meridional lines around the poles. In the case of the NMMB, the polar filter is acting only on time tendencies instead of on full atmospheric fields or their gradients, which eliminates some of the shortcomings of that approach (e.g., Takacs and Balgovind 1983; Purser 1988). However, reduced efficiency, caused by the global nature of Fourier transformations, remains as an unavoidable consequence of the large number of interprocessor communications that will only escalate on the future machines expected to incorporate tens of thousands of processors. This situation was perhaps best characterized by Randall et al. (1998), who described close zonal spacing of grid points near the poles as an "excessive spatial resolution, which demands increased and not necessarily useful computational resources," (p. 202) and considered that filters will "become prohibitively expensive at high resolutions, especially on modern parallel computers" (p. 202). Thus, the primary motivation of this project was to develop a version of the NMMB that will be free of polar filtering. The cubed sphere was selected because of its remarkable symmetry and the ability to naturally organize parallel computation.

The cubed sphere was suggested for application in numerical modeling by Sadourny (1972), as a

---

Corresponding author e-mail: Miodrag Rančić, miodrag.rancic@noaa.gov

DOI: 10.1175/MWR-D-16-0178.1

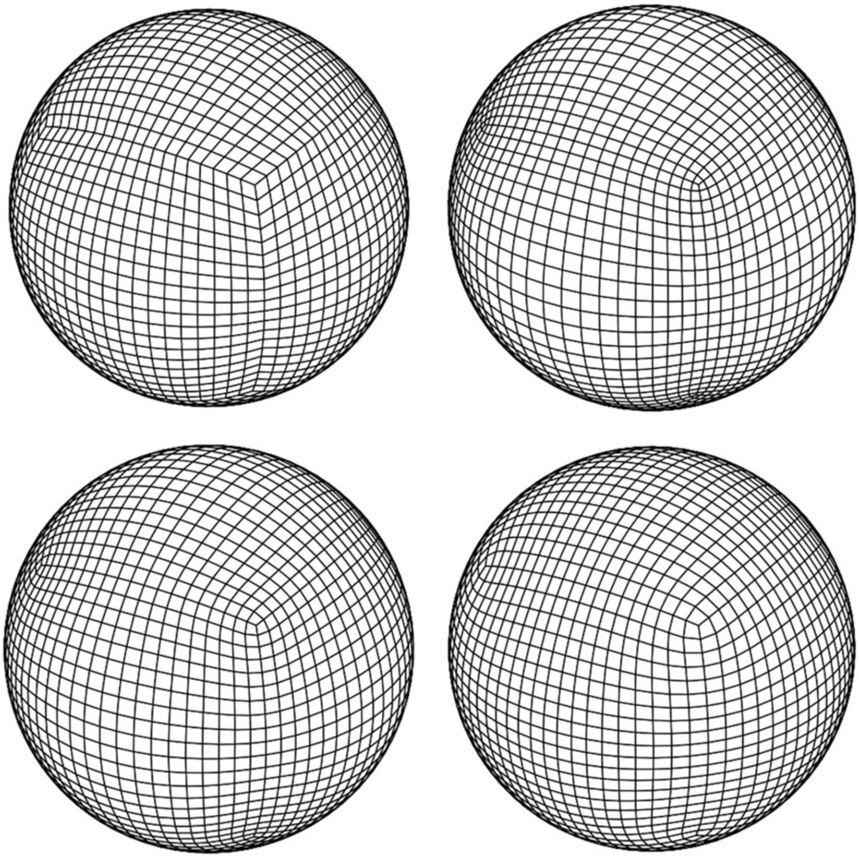

FIG. 1. (top left) Gnomonic cube, (top right) conformal cube, (bottom left) smooth (SM) cube, and (bottom right) UJ cube.

gnomonic cube (Fig. 1, top left) derived by a central projection from the sphere to a concentric cube. An ‘‘equiangular’’ version provides one of the most uniform mappings of the sphere possible, among those based on rectangular grid meshes, while the ‘‘equidistant’’ version results in somewhat increased resolution close to edges. The main problem with all versions of the gnomonic cube, regardless of the way their two coordinates are parameterized, is an angular discontinuity of the grid lines across the edges, which, together with eight singular corners, creates numerical problems, especially for application of Eulerian finite-differencing methods.

The papers of Ronchi et al. (1996), Rančić et al. (1996), and McGregor (1996), announced the resurrection of interest in the application of this geometry. Ronchi et al. (1996) suggested a new, grid overlapping approach on the gnomonic cube, while Rančić et al. (1996) and McGregor (1996) suggested numerical generation of coordinates over the cubed sphere, and designed a ‘‘conformal spherical cube’’ (i.e., such a modification of the gnomonic cube where the coordinate lines create conformal grid boxes except at the corners) (Fig. 1, top right). Such a conformal cubed sphere has very small grid boxes in the immediate vicinity of the corners, imposing too strict a linear stability condition. In the next refinement, Purser and Rančić (1998, hereafter PR98) suggested a ‘‘smoothed’’ (SM) cubed sphere (Fig. 1, bottom left), where the conformality requirement is relaxed while keeping a smooth transition of coordinates across edges.

Within this project we apply a novel cubed sphere with uniform Jacobians (UJ), shown in Fig. 1 (bottom right). The UJ cubed sphere supports continuity of derivatives of any order across the edges while having a more homogeneous resolution, which guarantees a sufficiently large time step.

The NMMB is a second-order, finite-differencing model, with an optional application of a fourth-order scheme for horizontal advection of tracers and momentum. It is an Eulerian model (though we plan to introduce a semi-Lagrangian treatment of tracers) with a strict enforcement of integral conservation constraints and a highly efficient handling of nonhydrostatic effects inherited from the regional NMMB. The next generation of numerical models will be running on global resolutions close to 1 km using tens of thousands of processors. In that situation, the simplicity, computational speed, and scalability of the numerical formulation become the primary desiderata, all of which recommends the NMMB-UJ, that is, the NMMB running in the UJ version of the cubed sphere, as a good candidate. The regional version of the NMMB has physics that is well tuned for high resolutions in operational runs over the contiguous U.S. domain (United States and surrounding seas) at a resolution of 4 km, which is an additional argument for considering an extension of that model with global coverage.

The NMMB-UJ was developed within the High Impact Weather Prediction Project (HIWPP), whose goal was to "improve time-zero to two-week weather prediction of Nature's most dangerous storms" (http://hiwpp.noaa.gov/).

In section 2 we give a brief introduction of the general curvilinear formalism. The derivation of the UJ cubed sphere with the analysis of its properties is described in section 3. In section 4 we present the analytical version of the model equations, which is followed by a description of their horizontal discretization in a general curvilinear coordinate frame in section 5. The demonstrations of model performance, including the computational aspects, two of the recommended HIWPP test cases, and an example of integration with full physics, are given in section 6. The paper concludes with discussion of the derived results. Conservation of dry mass and kinetic energy by the horizontal advection is demonstrated in the appendix.

2. Curvilinear formalism

In the case of a cubed sphere we deal with general curvilinear coordinates, and we here briefly review some of the related definitions. More details can be found, for example, in Rančić et al. (1996) and Zhang and Rančić (2007).

Using units of Earth radius for simplicity, let us denote with $X_k = (X, Y, Z)$ the components of the position vector $\mathbf{X}$ in a Cartesian absolute frame with the origin at the center of Earth. We express components of a wind vector $\mathbf{V}$ in this frame as $\dot{X}_k = (\dot{X}, \dot{Y}, \dot{Z})$, where $(\dot{\ })$ denotes the time derivative.

Let a pair $x^i = (x, y)$ define general curvilinear coordinates on the surface of a sphere, with the basis vectors $\mathbf{J}_1$ and $\mathbf{J}_2$ in the directions tangential to coordinate lines x and y, respectively, defined as

$$\mathbf{J}_1 = \frac{\partial \mathbf{X}}{\partial x} = \left(\frac{\partial X}{\partial x}, \frac{\partial Y}{\partial x}, \frac{\partial Z}{\partial x}\right)^{\mathrm{T}},$$

$$\mathbf{J}_2 = \frac{\partial \mathbf{X}}{\partial y} = \left(\frac{\partial X}{\partial y}, \frac{\partial Y}{\partial y}, \frac{\partial Z}{\partial y}\right)^{\mathrm{T}}, \qquad (1)$$

which we may conveniently combine into the single 3×2 Jacobian matrix:

$$\mathsf{J} = [\mathbf{J}_1, \mathbf{J}_2]. \qquad (2)$$

Covariant wind components, $u_i = (u, v)$, are defined by a scalar product of the absolute wind vector and the basis vectors of the curvilinear system:

$$\begin{bmatrix} u \\ v \end{bmatrix} = \begin{bmatrix} \mathbf{J}_1 \cdot \mathbf{V} \\ \mathbf{J}_2 \cdot \mathbf{V} \end{bmatrix} \equiv \mathsf{J}^{\mathrm{T}}\mathbf{V}. \qquad (3)$$

In our model, covariant winds are historic variables. *Contravariant* winds, $u^i = (\tilde{u}, \tilde{v})$, are defined as time derivatives of the curvilinear coordinates:

$$(\tilde{u}, \tilde{v}) = (\dot{x}, \dot{y}). \qquad (4)$$

The covariant metric tensor in curvilinear coordinates on the sphere is defined as

$$\mathsf{G} = \mathsf{J}^{\mathrm{T}}\mathsf{J} \equiv \begin{bmatrix} q_{11} & q_{12} \\ q_{21} & q_{22} \end{bmatrix}, \qquad (5)$$

where

$$q_{ij} \equiv \mathbf{J}_i \cdot \mathbf{J}_j, \quad i,j \in \{1,2\}. \qquad (6)$$

We denote by G the absolute scalar Jacobian of the transformation, defined as,

$$G = [\det(\mathsf{G})]^{1/2} = (\mathbf{J}_1 \times \mathbf{J}_2) \cdot \mathbf{n}, \qquad (7)$$

where $\mathbf{n} \equiv \mathbf{X}/|\mathbf{X}|$ is the unit normal vector on the surface of Earth.

The contravariant winds are related to the covariant winds via

$$\begin{bmatrix} \tilde{u} \\ \tilde{v} \end{bmatrix} = \mathsf{G}^{-1}\begin{bmatrix} u \\ v \end{bmatrix}, \qquad (8)$$

or, in Einstein tensor notation:

$$u^i = q^{ij}u_j, \qquad (9)$$

where the contravariant metric tensor has components written as

$$\mathsf{G}^{-1} = \begin{bmatrix} q^{11} & q^{12} \\ q^{21} & q^{22} \end{bmatrix}. \qquad (10)$$

For the discussion that follows it is important to recall definitions of basic horizontal vector operators in the curvilinear coordinates: divergence D, and the gradient and the Laplacian of a scalar A, respectively, as

$$D = \frac{1}{G}\left(\frac{\partial \tilde{u}G}{\partial x} + \frac{\partial \tilde{v}G}{\partial y}\right), \tag{11}$$

$$\nabla A = \left(\frac{\partial A}{\partial x}, \frac{\partial A}{\partial y}\right)^{\mathrm{T}}, \quad \text{and} \tag{12}$$

$$\nabla^2 A = \frac{1}{G}\left\{\frac{\partial}{\partial x}\left[G\left(q^{11}\frac{\partial A}{\partial x} + q^{12}\frac{\partial A}{\partial y}\right)\right] + \frac{\partial}{\partial y}\left[G\left(q^{21}\frac{\partial A}{\partial x} + q^{22}\frac{\partial A}{\partial y}\right)\right]\right\}. \tag{13}$$

3. Mappings with the UJ property

The principal defect of the conformal cubed sphere introduced by Rančić et al. (1996) and McGregor (1996) was the exceptionally small grid spacing around each corner singularity, so a remedial generalization of that mapping was proposed in PR98. There, we considered the implications of the solution minimizing the variational principle for a mapping covering the unit sphere,

$$\mathscr{L} = \frac{1}{2}\iint [(|\mathbf{J}_1|^2 + |\mathbf{J}_2|^2) + aG^2 + \Lambda(|\mathbf{X}|^2 - 1)]\,dx\,dy, \tag{14}$$

whose solution was shown to revert to the conformal case in the special limit of the Jacobian-smoothing term, aG^2, vanishing, but to generate a new and more equitably resolving family of mappings when the constant "smoothing coefficient," a, was prescribed to be strictly positive. It is this "smoothed cubed-sphere" (SM) family that serves as the main inspiration for the present extension, actually the limiting case, $a \to \infty$, which led to our uniform Jacobian (UJ) grid. It is, therefore, worth briefly reviewing the principles that underlie this variational construction, its relationship to other cubed-sphere geometries, and the manner in which a version of the UJ cubed sphere emerges from it.

Since we are interested in the minimum value of the integral in (14), any constant multiple of the scalar Jacobian, G, of the mapping can be added to the integrand without changing the solution, owing to the integral of G being 4π regardless of the details of the continuous mapping. Using this property the first two terms of the integrand can be replaced by the square of the norm of the purely anisotropic (trace free and symmetric) part of a kind of "strain tensor" of the mapping, as one can verify by considering a local Cartesian tangent coordinate frame, (x_τ, y_τ), and observing then that, with respect to this frame at the tangent point

$$G = \frac{\partial x_\tau}{\partial x}\frac{\partial y_\tau}{\partial y} - \frac{\partial y_\tau}{\partial x}\frac{\partial x_\tau}{\partial y}. \tag{15}$$

Our anisotropic symmetric strain tensor $\mathbf{e}$ at the tangent point can be defined as

$$\mathbf{e} = \begin{bmatrix} e_{11} & e_{12} \\ e_{12} & -e_{11} \end{bmatrix}, \tag{16}$$

with

$$e_{11} = \frac{1}{2}\left(\frac{\partial x_\tau}{\partial x} - \frac{\partial y_\tau}{\partial y}\right), \quad e_{12} = \frac{1}{2}\left(\frac{\partial y_\tau}{\partial x} + \frac{\partial x_\tau}{\partial y}\right), \tag{17}$$

such that this tensor's squared norm,

$$e^2 \equiv \|\mathbf{e}\|^2 = 2(e_{11}^2 + e_{12}^2), \tag{18}$$

can be expanded to show that

$$\frac{1}{2}(|\mathbf{J}_1|^2 + |\mathbf{J}_2|^2) = \frac{1}{2}\left[\left(\frac{\partial x_\tau}{\partial x}\right)^2 + \left(\frac{\partial x_\tau}{\partial y}\right)^2 + \left(\frac{\partial y_\tau}{\partial x}\right)^2 + \left(\frac{\partial y_\tau}{\partial y}\right)^2\right] = e^2 + G. \tag{19}$$

Thus, we can legitimately interpret the variational principle of PR98 [our (14)] defining the smooth polyhedral mapping as being modeled on a continuous elasticity model in which a part of the elastic energy (the integral of e^2) derives from the anisotropic component of deformation of the medium and the other part of the elastic energy (the integral of $1/2aG^2$) derives from the horizontal compression or expansion of the two-dimensional medium in which the map coordinates (x, y) are imagined to be materially embedded. We compare this construction method with the conceptually similar "spring dynamics" method proposed by Tomita et al. (2001, 2002) which is also motivated by a principle of minimizing elastic energy, but in that case, the energy of a discrete collection of springs forming the computational lattice elements. The coefficient a denotes the ratio of the two kinds of elastic modulus; when $a = 0$, we showed in PR98 that the resulting minimum-energy solutions (they are not unique) would be of the conformal kind with singular Jacobians at the corner singularities of the mapping. For finite a, where the departures from uniformity of the Jacobian G are penalized, we were able to get smooth and more uniform mappings. The other extreme of the variational principle of PR98 occurs when we consider the limiting case where $a \to \infty$. This limit is equivalent to replacing the second quadratic integrand term with a new Lagrange multiplier constraint to enforce the exact uniformity of the Jacobian to its average value G_0:

$$\mathscr{L} = \frac{1}{2}\iint\left[(|\mathbf{J}_1|^2 + |\mathbf{J}_2|^2) - \frac{2}{G_o}K(G - G_0) + \Lambda(|\mathbf{X}|^2 - 1)\right] dx\,dy. \tag{20}$$

This is a variational definition of a smooth uniform-Jacobian (UJ) polyhedral mapping. In the elastic analogy it corresponds to a horizontally incompressible elastic membrane whose energy derives entirely from the integrated squared norm of our traceless strain tensor. The Euler–Lagrange equations (Lovelock and Rund 1975) corresponding to Eqs. (2) and (3) of PR98 are obtained by considering independent variations with respect to the components of $\mathbf{X}$, the multiplier field K, and the multiplier field Λ. We find that

$$\frac{\partial^2\mathbf{X}}{\partial x^2} + \frac{\partial^2\mathbf{X}}{\partial y^2} = \nabla K + \Lambda\mathbf{X}, \tag{21}$$

$$G = G_o, \tag{22}$$

$$|\mathbf{X}| = 1, \tag{23}$$

where the gradient acting on K is the embedded Cartesian two-dimensional tangent-space operator. Thus, in the elastostatic analogy, K serves as a kind of 2D "pressure" needed to balance the horizontal "elastic" forces of the first term of (20) in order to maintain the constraint of a uniform Jacobian, while the vertical force term containing Λ serves to balance the radial elastic force term to keep the mapping solution on the surface of the unit sphere.

An approximation to the UJ-cube mapping defined by this new variational principle is obtained by a splitting of the contributions as follows. First, we ignore the "K" constraint and simply obtain the perfectly smooth (except for eight corner singularities) conformal cubic intermediate solution [see Rančić et al. (1996), for a description of the method by which a conformal cubic mapping is efficiently and accurately constructed]; then we "switch on" the uniform Jacobian constraint by seeking the most direct irrotational perturbation of the mapping that brings it into consistency with the uniform Jacobian constraint. Just as the most direct force opposing the elasticity terms in the final uniform Jacobian state is known to be a gradient of a scalar (K), the most direct projection onto the abstract space of uniform Jacobian mappings from any initial nonuniform-Jacobian mapping (such as our conformal intermediate state) is via a pure gradient motion. The two-stage construction defined in Purser and Rančić (2011) shows how such an irrotational position perturbation is obtained, using a velocity potential integrated over a pseudo-time to ensure that the logarithm of the Jacobian tends directly to perfect uniformity.

In the next several paragraphs we will compare the UJ cubed sphere with the SM and equiangular gnomonic cubed spheres.

The SM cubed sphere was derived by smoothing of the conformal cubed sphere, controlled by the smoothing coefficient, a, that could take values from 0 (conformal cube) to a practical limit of about 100. The SM cubed sphere provided a better ratio between the minimum and the maximum grid distance (hereafter "homogeneity") than the conformal cubed sphere, but also extended the area around the corners where the coordinate lines were not orthogonal. Homogeneity of the SM cubed sphere, as a function of smoothing coefficient a, is shown in Fig. 2a, calculated for a resolution of $96 \times 4 = 384$ grid boxes around the equator (roughly 104 km). Homogeneity of the UJ cubed sphere for a resolution of 104 km was found to be about 0.7074, and is also plotted in Fig. 2a, along with the homogeneity of the equiangular gnomonic cubed sphere (0.7129). The dependence of homogeneity with resolution on the UJ and gnomonic cubed spheres is shown in Fig. 2b. The UJ has nearly constant homogeneity, which is approaching to that of the gnomonic with increase of resolution, but without angular discontinuity across the edges. Note that if the homogeneity was expressed using the surface area of grid boxes instead of their edges, then it would be equal to 1 on the UJ cubed sphere.

Figure 3 shows respectively the orthogonality, the angular skewness, and the aspect ratio (e.g., Weller 2014), calculated for SM, UJ, and gnomonic cubed spheres. The "orthogonality" is measured in the centers of grid boxes and represents the departure of intersection angle between x and y coordinates from 90°. The "angular skewness" of a grid box is defined as a normalized maximal departure from 90° of all angles within the box, that is,

$$\max\left[\frac{\theta_{\max} - 90}{90}, \frac{90 - \theta_{\min}}{90}\right]. \tag{24}$$

The "aspect ratio" is defined as a ratio of the minimum to the maximum gridbox edge. We calculate these measures in the map space, and in order to avoid repetition, present here only the top-right quarter of the cube

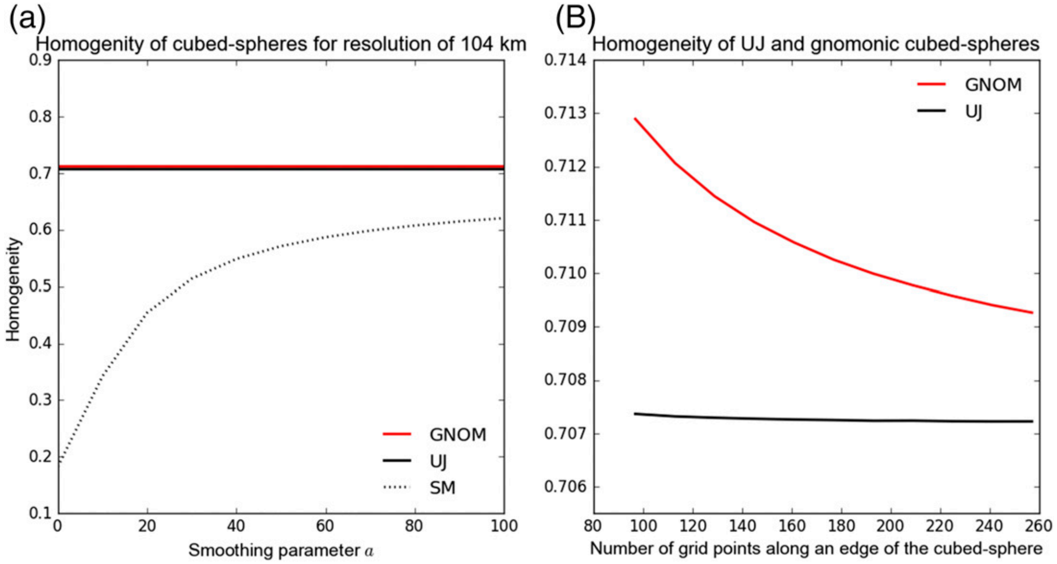

FIG. 2. (a) Homogeneity of SM, UJ, and gnomonic cubed spheres calculated for a resolution of 104 km. The UJ and gnomonic have constant homogeneity, and for SM it is a function of a smoothing coefficient a. (b) Homogeneity of gnomonic and UJ cubed spheres calculated for several increasing resolutions starting from 104 km.

face, since the other quarters are symmetrical. The smoothing coefficient a of the SM cubed sphere was 20. The cubed spheres have resolution of 160×160 grid boxes on each face.

From Fig. 3 it follows that the UJ has the best orthogonality and skewness (closer to zero in the larger area) especially in comparison with the gnomonic cubed sphere. However, surprisingly, the SM cubed sphere has the best aspect ratio (closer to 1), and the UJ cubed sphere behaves similarly to the gnomonic, though with somewhat tighter area where the aspect ratio is close to 1.

4. Continuous equations

The NMMB is a nonhydrostatic model of the atmosphere, developed and described in Janjić et al. (2001), Janjić (2003), and elsewhere. It is formulated using a hydrostatic pressure, mass-coordinate-based system, introduced by Laprise (1992). The longitude–latitude version of the model is described in detail in Janjić and Gall (2012), which we loosely follow in this section.

Hydrostatic pressure π at some geopotential level Φ is defined as the weight of the column of air, that is,

$$\pi = \pi_T + \int_{\Phi}^{\Phi_T} \rho \, d\Phi , \tag{25}$$

where π_T and Φ_T denotes values at the top of model's atmosphere.

The model uses the hybrid coordinate system suggested by Eckermann (2009), where hydrostatic pressure is calculated from

$$\pi = \pi_T + \sigma_1(\eta)\Pi + \sigma_2(\eta)(\pi_S - \pi_T) . \tag{26}$$

The hybrid system (26) is a generalized version of the hydrostatic sigma system, with an extra term, $\sigma_1 \Pi$; σ_1 is equal to 0 at the top and bottom of the atmosphere, and Π is a conveniently selected constant. The term σ_2 takes a value 0 at the top and 1 at the bottom of the model's atmosphere, where hydrostatic pressure is π_S.

From the definition of hydrostatic pressure, (25) follows a "hypsometric equation" below, which is used to formulate hydrostatic pressure-based equations for the nonhydrostatic atmosphere:

$$\frac{\partial \Phi}{\partial \pi} = -\frac{RT}{p} . \tag{27}$$

Note that here p is true pressure. Assuming that both hydrostatic pressure and geopotential are functions of the new hybrid coordinate η, the above equation may be rewritten as

$$\frac{\partial \Phi}{\partial \eta} = -\frac{RT}{p} m , \tag{28}$$

where "hydrostatic mass" m is defined by

$$m = \frac{\partial \pi}{\partial \eta} . \tag{29}$$

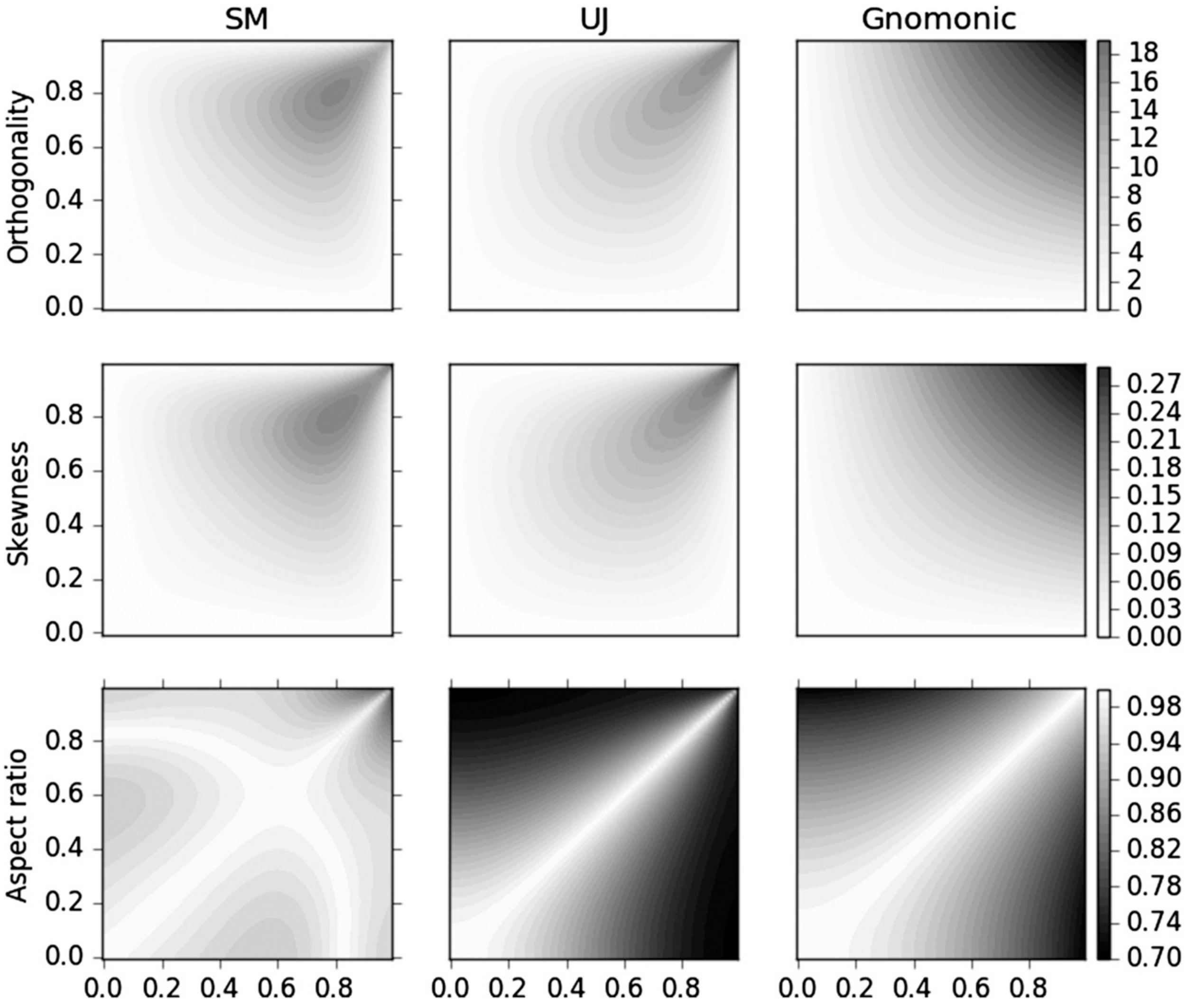

FIG. 3. Orthogonality (°), angular skewness, and aspect ratio for SM, UJ, and equiangular gnomonic cubed spheres, shown in the top-right quarter of a cube's face expressed in the map space.

Prognostic equations to solve for momentum (u and v), temperature (T), and hydrostatic mass (m) are, respectively,

$$\frac{\partial u}{\partial t} = -\left(\tilde{u}\frac{\partial \mathbf{V}}{\partial x} + \tilde{v}\frac{\partial \mathbf{V}}{\partial y}\right)\cdot \mathbf{J}_1 - \dot{\eta} m \frac{\partial u}{\partial \pi} - (1+\varepsilon)\frac{\partial \Phi}{\partial x} - \frac{RT}{p}\frac{\partial p}{\partial x}, \qquad (30)$$

$$\frac{\partial v}{\partial t} = -\left(\tilde{u}\frac{\partial \mathbf{V}}{\partial x} + \tilde{v}\frac{\partial \mathbf{V}}{\partial y}\right)\cdot \mathbf{J}_2 - \dot{\eta} m \frac{\partial v}{\partial \pi} - (1+\varepsilon)\frac{\partial \Phi}{\partial y} - \frac{RT}{p}\frac{\partial p}{\partial y}, \qquad (31)$$

$$\frac{\partial T}{\partial t} = -\left(\tilde{u}\frac{\partial T}{\partial x} + \tilde{v}\frac{\partial T}{\partial y}\right) - \dot{\eta} m \frac{\partial T}{\partial \pi} + \frac{1}{c_p}\frac{RT}{p}\omega, \qquad (32)$$

$$\frac{\partial m}{\partial t} = -\frac{1}{G}\left[\frac{\partial}{\partial x}(\tilde{u}Gm) + \frac{\partial}{\partial y}(\tilde{v}Gm)\right] - \frac{\partial}{\partial \eta}(\dot{\eta} m). \qquad (33)$$

We express the total derivatives using the formulation introduced by Kasahara (1974) and adjusted here for the curvilinear framework; c_p is specific heat at constant pressure, R is the gas constant of dry air, and T is temperature.

In addition, a nonhydrostatic model needs to describe the time change of vertical wind in geometrical height w and the true pressure p, which in the NMMB is solved in a unique, efficient diagnostic manner that avoids overspecification of variables, described in detail in Janjić et al. (2001). We here only give a brief recapitulation of this procedure.

First, observe that from (28) one can calculate geopotential as

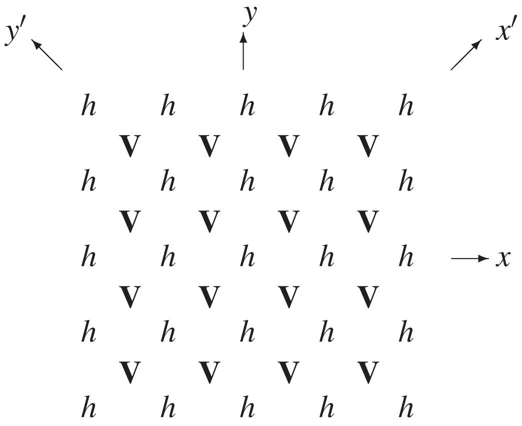

FIG. 4. B grid and definition of axes.

$$\Phi = \Phi_S - \int_{\eta_S}^{\eta} \frac{RT}{p} m \, d\eta . \tag{34}$$

Second, from the definition of geopotential, one can calculate the vertical wind w as

$$w \equiv \frac{dz}{dt} = \frac{1}{g}\left(\frac{\partial \Phi}{\partial t} + \tilde{u}\frac{\partial \Phi}{\partial x} + \tilde{v}\frac{\partial \Phi}{\partial y} + \dot{\eta} m \frac{\partial \Phi}{\partial \pi}\right). \tag{35}$$

Third, once w is found, a similar procedure can be applied to update vertical acceleration dw/dt:

$$\frac{dw}{dt} = \frac{\partial w}{\partial t} + \tilde{u}\frac{\partial w}{\partial x} + \tilde{v}\frac{\partial w}{\partial y} + \dot{\eta} m \frac{\partial w}{\partial \pi}. \tag{36}$$

To explain the calculation of the true pressure, recall that the vertical equation of motion is

$$\begin{aligned}\frac{dw}{dt} &= -\frac{RT}{p}\frac{\partial p}{\partial z} - g \\ &= -g\left(\frac{RT}{p}\frac{\partial p}{\partial \Phi} + 1\right) \\ &= -g\left(\frac{RT}{p}\frac{\partial p}{\partial \pi}\frac{\partial \pi}{\partial \Phi} + 1\right).\end{aligned} \tag{37}$$

Finally, by applying (27) to the term $\partial \pi / \partial \Phi$ in the last expression, vertical acceleration becomes

$$\frac{dw}{dt} = g\left(\frac{\partial p}{\partial \pi} - 1\right). \tag{38}$$

Using this equation, Janjić et al. (2001) expressed the increment of true pressure relative to hydrostatic as

$$\frac{\partial p}{\partial \pi} = 1 + \varepsilon , \tag{39}$$

where ε denotes vertical acceleration normalized by gravity:

$$\varepsilon = \frac{1}{g}\frac{dw}{dt}. \tag{40}$$

Note that once vertical acceleration is found from (34), (35), and (36), pressure can be diagnosed from (39) as

$$p = \int_0^{\eta} (1 + \varepsilon) m \, d\eta . \tag{41}$$

The ω in the thermodynamic equation is defined as

$$\begin{aligned}\omega = {} & \frac{\partial p}{\partial t} - (1+\varepsilon)\frac{\partial \pi}{\partial t} + \left(\tilde{u}\frac{\partial p}{\partial x} + \tilde{v}\frac{\partial p}{\partial y}\right) \\ & - \frac{(1+\varepsilon)}{G}\int_0^{\eta}\left(\frac{\partial G\tilde{u}m}{\partial x} + \frac{\partial G\tilde{v}m}{\partial y}\right) d\eta .\end{aligned} \tag{42}$$

The hydrostatic continuity equation is used to calculate the local time change of hydrostatic pressure and to diagnose the vertical mass flux ($\dot{\eta}m$). As can be verified by inspection, the nonhydrostatic system reduces to the hydrostatic one when the nonhydrostatic correction factor ε is equal to zero.

In the following section we describe discretization of the dynamic equations discussed in this section, with the emphasis on those elements that are unique to the geometry of the cubed sphere, such as spatial differencing and treatment of the corners, while leaving out details that can be found elsewhere, for example, in Janjić and Gall (2012).

5. Discrete equations

The NMMB-UJ uses the Arakawa B grid (Fig. 4) with h points that carry scalar variables and coincide with the horizontal position of vertical mass fluxes, arranged along edges of the cube, which was suggested in Rančić et al. (1996) and applied in the global Eta model of Zhang and Rančić (2007). The normal (x, y) and the diagonal (x', y') directions on the B grid, which will be used in the descriptions that follow, are shown in Fig. 4. The model uses the Lorenz (1960) arrangement of variables in the vertical, where both temperature and winds are placed at the middle of vertical layers and vertical mass fluxes are at interfaces. The true pressure p and geopotential Φ are also located at interfaces, while the vertical wind w resides in the middle of layers located at h points.

To avoid double calculation along common edges, which may lead to separation of solutions along edges and affect scalability, each face of the cubed sphere was assigned only two edges along which we perform calculation and the values at two other edges are provided through message exchange. Two of the cube corners in this way could be left out of the calculation unless care is taken to assign them to one of the faces to which they belong.

Alternatively, one can organize the computation so that each face includes all of its edges and corners in the calculation. This increases the computational load, but reduces the overall amount of communications, and simplifies formulation of communication subroutines. We tested both methods, but the advantages of one or the other were not conclusive.

Following logistics from the NMMB on the longitude–latitude grid, the prognostic equations are advanced in time using second-order Adams–Bashforth differencing, with a few exceptions: the adjustment terms are solved using the forward–backward scheme and the vertical advections and terms responsible for vertical propagation of sound waves are treated implicitly. Implicit treatment of vertical advection allows the vertical grid spacing, especially close to the ground, to be kept sufficiently fine, without the need to reduce the time step which would adversely affect the overall efficiency.

The focus here is on horizontal discretization, where the longitude–latitude orthogonal coordinate frame is replaced by the general curvilinear formulation applied on the cubed sphere. Vertical space differencing remains the same as in the original NMMB described, along with more details of the time-differencing strategy in Janjić and Gall (2012).

In this paper we use the following notation for finite differencing:

- A difference between two successive values of a variable A in the direction of a coordinate axis s will be denoted as $\Delta_s A$. We will mainly use this notation to denote vertical differencing.
- An averaging of two successive values of a variable A in the direction of a coordinate axis s will be denoted by $\overline{A}^s$.
- A discrete gradient of the variable A in the direction of coordinate axis s will be denoted as $\delta_s A \equiv \Delta A/\Delta s$, where Δs is the increment of coordinate s in map space.

a. Adjustment terms

We define a finite-difference approximation of the horizontal part of the continuity equation (33) on the B grid from Fig. 4 as

$$\frac{\partial m}{\partial t} = -\frac{1}{G}\left[\frac{2}{3}(\delta_x U + \delta_y V) + \frac{1}{3}(\delta_{x'} U' + \delta_{y'} V')\right]. \tag{43}$$

Normal fluxes (U, V) in the direction of axes (x, y) in Fig. 4, are defined as

$$\begin{aligned} U &= \overline{m}^x \tilde{u} \overline{G}^y, \\ V &= \overline{m}^y \tilde{v} \overline{G}^x. \end{aligned} \tag{44}$$

Diagonal fluxes (U', V') in the direction of axes (x', y') in Fig. 4, are defined as

$$\begin{aligned} U' &= \overline{m}^{x'} \frac{\sqrt{2}}{2}(\tilde{u} + \tilde{v})G, \\ V' &= \overline{m}^{y'} \frac{\sqrt{2}}{2}(-\tilde{u} + \tilde{v})G. \end{aligned} \tag{45}$$

Here

$$m \equiv \Delta_\eta \pi, \tag{46}$$

where π is hydrostatic pressure and η is the vertical coordinate as before.

The pressure gradient force from (30) and (31) is approximated as

$$\begin{aligned} \left(\frac{\partial u}{\partial t}\right)_{\text{pgf}} = -\frac{1}{\overline{m}^{xy}}\Bigg[&(1+\varepsilon)\left\langle \frac{2}{3}\overline{\overline{m}^x \delta_x \overline{\Phi}^\eta}^y + \frac{1}{3}\frac{\sqrt{2}}{2}(\overline{m}^{x'}\delta_{x'}\overline{\Phi}^\eta - \overline{m}^{y'}\delta_{y'}\overline{\Phi}^\eta)\right\rangle \\ &+ \left\langle \frac{2}{3}\overline{\overline{\alpha m}^x \delta_x \overline{p}^\eta}^y + \frac{1}{3}\frac{\sqrt{2}}{2}(\overline{\alpha m}^{x'}\delta_{x'}\overline{p}^\eta - \overline{\alpha m}^{y'}\delta_{y'}\overline{p}^\eta)\right\rangle\Bigg], \end{aligned} \tag{47}$$

$$\begin{aligned} \left(\frac{\partial v}{\partial t}\right)_{\text{pgf}} = -\frac{1}{\overline{m}^{xy}}\Bigg[&(1+\varepsilon)\left\langle \frac{2}{3}\overline{\overline{m}^y \delta_y \overline{\Phi}^\eta}^x + \frac{1}{3}\frac{\sqrt{2}}{2}(\overline{m}^{x'}\delta_{x'}\overline{\Phi}^\eta + \overline{m}^{y'}\delta_{y'}\overline{\Phi}^\eta)\right\rangle \\ &+ \left\langle \frac{2}{3}\overline{\overline{\alpha m}^y \delta_y \overline{p}^\eta}^x + \frac{1}{3}\frac{\sqrt{2}}{2}(\overline{\alpha m}^{x'}\delta_{x'}\overline{p}^\eta + \overline{\alpha m}^{y'}\delta_{y'}\overline{p}^\eta)\right\rangle\Bigg]. \end{aligned} \tag{48}$$

Here, α, proportional to specific volume, is defined as

$$\alpha = \frac{RT}{\overline{p}^\eta}. \tag{49}$$

A consistent hydrostatic horizontal part of the energy transformation $\omega\alpha$ term can be expressed as

$$\begin{aligned} \left(\frac{\partial T}{\partial t}\right)_{\omega_h \alpha} = \frac{1}{mG}\Bigg[&\frac{2}{3}\left\langle \overline{\overline{\alpha}^x U \delta_x \overline{p}^\eta}^x + \overline{\overline{\alpha}^y V \delta_y \overline{p}^\eta}^y \right\rangle \\ &+ \frac{1}{3}\left\langle \overline{\overline{\alpha}^{x'} U \delta_{x'} \overline{p}^\eta}^{x'} + \overline{\overline{\alpha}^{y'} V \delta_{y'} \overline{p}^\eta}^{y'} \right\rangle\Bigg]. \end{aligned} \tag{50}$$

The technique for preventing separation of gravity waves on the elementary C grids of Mesinger (1973) and Janjić

(1974) is turned off at the corners of the cubed sphere and modified in their vicinity to ensure mass conservation.

By ignoring terms associated with the third wind component, the Coriolis force is defined as

$$\left(\frac{\partial u}{\partial t}\right)_{\text{cor}} = 2\Omega\tilde{v}\mathscr{J}_{xy}(X, Y),$$
$$\left(\frac{\partial v}{\partial t}\right)_{\text{cor}} = -2\Omega\tilde{u}\mathscr{J}_{xy}(X, Y), \qquad (51)$$

where Ω is the angular speed of Earth's rotation and $\mathscr{J}$ denotes Jacobian of the absolute coordinates with respect to the map space.

b. *Nonlinear momentum advection scheme*

The nonlinear momentum advection scheme is defined using the "vector projected method" of Rančić et al. (2008). Instead of the Janjić (1984) nonlinear momentum scheme, which conserves a C-grid vorticity (and enstrophy) on the semistaggered grid, we use the Arakawa (1972) scheme, which conserves a finite-difference analog of vorticity defined as an average of C- and E-grid vorticities. This represents one of two major departures, in this case a slight degradation, in comparison to the original NMMB model, because the Janjić (1984) momentum advection scheme better restricts flow of nonlinear energy toward the smallest resolvable scales. Still, the Arakawa (1972) scheme does not produce spurious nonlinear interactions between short and long scales, and is much easier to apply in a general curvilinear formulation, especially on the grid topology of the cubed sphere, because of its fully isotropic formulation. In addition, in comparison with the B-grid version of the Janjić (1984) scheme, the Arakawa (1972) scheme represents a more efficient choice.

In vector form, the continuous horizontal momentum terms are defined as

$$\left(\frac{\partial \mathbf{V}}{\partial t}\right)_{\text{adv}} = -\left(\tilde{u}\frac{\partial \mathbf{V}}{\partial x} + \tilde{v}\frac{\partial \mathbf{V}}{\partial y}\right). \qquad (52)$$

Discretizing this equation in the spirit of Arakawa (1966) conservation principles and using both normal and diagonal directions, results in

$$\left(\frac{\partial \mathbf{V}}{\partial t}\right)_{\text{adv}} = -\frac{1}{\overline{\overline{hG}}^{xy}}\left[\frac{2}{3}\left(\overline{\mathscr{U}\delta_x \mathbf{V}}^{x} + \overline{\mathscr{V}\delta_y \mathbf{V}}^{y}\right)\right.$$
$$\left.+\frac{1}{3}\left(\overline{\mathscr{U}'\delta_{x'} \mathbf{V}}^{x'} + \overline{\mathscr{V}'\delta_{y'} \mathbf{V}}^{y'}\right)\right]. \qquad (53)$$

The fluxes in these expressions are defined as

$$\mathscr{U} = \overline{U}^{xy}, \quad \mathscr{V} = \overline{V}^{xy}, \qquad (54)$$
$$\mathscr{U}' = \overline{U'}^{xy}, \quad \mathscr{V}' = \overline{V'}^{xy}, \qquad (55)$$

where U, V, U', and V' are defined in (44) and (45).

In Rančić et al. (2008), Eq. (53) was projected onto normal directions of map space in order to find tendencies of covariant winds. In this paper, we project this vector equation onto coordinates of the absolute coordinate system, (X, Y, Z), and solve for time tendencies of the absolute winds, $(\dot{X}, \dot{Y}, \dot{Z})$, keeping the form of the scheme identical to (53) for each of these components. Once the time tendencies of wind components in the absolute frame are found, we calculate tendencies of the covariant winds, our historic variables, from

$$\left(\frac{\partial u}{\partial t}\right)_{\text{adv}} = \frac{\partial \mathbf{V}}{\partial t}\cdot \mathbf{J}_1,$$
$$\left(\frac{\partial v}{\partial t}\right)_{\text{adv}} = \frac{\partial \mathbf{V}}{\partial t}\cdot \mathbf{J}_2. \qquad (56)$$

This method involves solving three instead of two equations, but is much simpler to apply than the original vector projected method. Some minor modifications of the scheme are applied close to the corners of the cube in order to preserve conservation of kinetic energy, which is discussed in the appendix.

The fourth-order version of the horizontal advection schemes is also included in NMMB-UJ as an option, following Janjić et al. (2011).

c. *Horizontal diffusion*

Nonlinear horizontal diffusion of a variable A may be expressed as

$$\left(\frac{\partial A}{\partial t}\right)_{\text{diff}} = \nabla\cdot(K\nabla A). \qquad (57)$$

Following Smagorinsky (1963), the coefficient of the horizontal diffusion can be expressed as

$$K = C_D\chi, \qquad (58)$$

where C_D is a Smagorinsky constant and χ represents a scalar norm of the horizontal trace-free flow deformation tensor $\boldsymbol{\chi}$ (analogous to the anisotropic strain in section 2). An exact covariant expression for the scalar χ in general curvilinear coordinates is given, in tensor notation, by

$$\chi = \left[\frac{1}{2}\chi_{ij}\chi_{kl}q^{ik}q^{jl}\right]^{1/2}, \qquad (59)$$

where the covariant tensor χ_{ij} is defined as

$$\chi_{ij} = u_{i|j} + u_{j|i} - q_{ij}D. \qquad (60)$$

Here, D is the horizontal divergence defined by (11); q_{ij} and q^{ij} are the covariant and contravariant metric tensors given by (6) and (10), respectively; and $u_{i|j}$ denotes the "covariant derivative" of $u_i = (u, v)$ with respect to $x^j = (x, y)$ (for general definitions of covariant differentiation, see, e.g., Synge and Schild 1949). This is a tensor that, in our case, could be written using the pair of Jacobian vectors $\mathbf{J}_i$:

$$u_{i|j} = \frac{\partial u_i}{\partial x^j} - u^k \mathbf{J}_k \cdot \frac{\partial \mathbf{J}_j}{\partial x^i}. \qquad (61)$$

If $\boldsymbol{\chi}$ were evaluated in local Cartesian coordinates, then,

$$\boldsymbol{\chi} = \begin{bmatrix} \chi_{11} & \chi_{12} \\ \chi_{12} & -\chi_{11} \end{bmatrix}, \qquad (62)$$

and

$$\chi = [\chi_{11}^2 + \chi_{12}^2]^{1/2}, \qquad (63)$$

but an adequate approximation to the pair of arguments in (63), which we have used to define χ in our experiments, takes

$$\chi_{11} \approx \frac{1}{G}\left(\frac{\partial G\tilde{u}}{\partial x} - \frac{\partial G\tilde{v}}{\partial y}\right),$$
$$\chi_{12} \approx \frac{1}{G}\left(\frac{\partial v}{\partial x} + \frac{\partial u}{\partial y}\right). \qquad (64)$$

The diffusion in our model on the B grid is discretized as

$$\nabla \cdot (K\nabla A) = \frac{C_D}{G}[\delta_x(\chi G\tilde{u}_A) + \delta_y(\chi G\tilde{v}_A)], \qquad (65)$$

where in the case that A is a scalar variable:

$$\chi G\tilde{u}_A = (Gq^{11})\overline{\chi}^x \delta_x A + \overline{(Gq^{12})\overline{\chi}^y \delta_y A}^{xy},$$
$$\chi G\tilde{v}_A = \overline{(Gq^{21})\overline{\chi}^x \delta_x A}^{xy} + (Gq^{22})\overline{\chi}^y \delta_y A. \qquad (66)$$

In the case of momentum, diffusion is applied to each of the absolute wind components $\dot{X}_k$ discretized as

$$\chi G\tilde{u}_{\dot{X}_k} = (Gq^{11})\overline{\chi}^y \delta_x \dot{X}_k + \overline{(Gq^{12})\overline{\chi}^x \delta_y \dot{X}_k}^{xy},$$
$$\chi G\tilde{v}_{\dot{X}_k} = \overline{(Gq^{21})\overline{\chi}^y \delta_x \dot{X}_k}^{xy} + (Gq^{22})\overline{\chi}^x \delta_y \dot{X}_k. \qquad (67)$$

Metrics Gq^{11}, Gq^{12}, etc., in these formulas are defined on the corresponding cross sections between h and $\mathbf{V}$ points. (On the UJ cubed sphere, the Jacobian G is equal everywhere except at the corner points that carry scalars. Thus, in principle, G could be ignored in all expressions for diffusion of winds. However, we still keep it here everywhere for consistency.) Once the diffusion of each of the absolute wind components is found, the tendencies of covariant winds are updated by transforming diffusion of absolute winds back to covariant winds:

$$\left(\frac{\partial u}{\partial t}\right)_{\text{diff}} = \nabla \cdot [(K\nabla \mathbf{V}) \cdot \mathbf{J}_1],$$
$$\left(\frac{\partial v}{\partial t}\right)_{\text{diff}} = \nabla \cdot [(K\nabla \mathbf{V}) \cdot \mathbf{J}_2]. \qquad (68)$$

If we need to use a linear instead of nonlinear diffusion, as in an idealized convection supercell test case shown in the next section, then χ is set to 1, and constant C_D is chosen differently than in the case of nonlinear diffusion.

In principle, the diagonal directions also should have been included in the definition of horizontal diffusion for consistency with the rest of the dynamics. However, this would increase the expense of calculation without clear benefit for performance and we postpone that for now.

d. Advection of tracers

Horizontal advection of a tracer ψ defined at scalar points can be discretized as

$$\frac{\partial \psi}{\partial t} = -\frac{1}{mG}\left[\frac{2}{3}(\overline{U\delta_x\psi}^x + \overline{V\delta_y\psi}^y)\right.$$
$$\left.+\frac{1}{3}(\overline{U'\delta_{x'}\psi}^{x'} + \overline{V'\delta_{y'}\psi}^{y'})\right]. \qquad (69)$$

We demonstrate in the appendix global conservation of both the first and second moments of scalar ψ. Conservation of the second moment allows us, just as in the original NMMB, to actually advect a square root of the scalar, $\sqrt{\psi}$, which translates to its positive definiteness. However, the scheme does not have a mechanism to prevent over- and undershoots, and therefore we apply an a posteriori procedure in order to preserve monotonicity of the solution.

Since we plan to introduce a semi-Lagrangian scheme for all passive tracers, we supplied the NMMB-UJ with a state-of-the-art approach for monotonization and a consequent restoration of the global first moment of each advected field, somewhat more advanced than the one in the original NMMB. After application of horizontal and vertical advection schemes to a tracer ψ, while the first moment of tracer is conserved, there are no guarantees that unrealistic overshoots/undershoots, known as Gibbs oscillations, will not appear. Therefore, the first intervention consists of applying the filter that will remove these

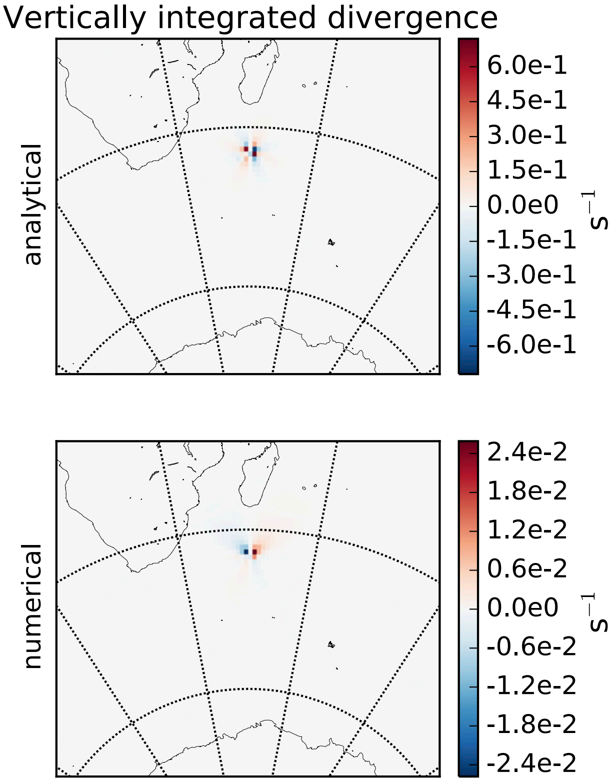

FIG. 5. False generation of vertically integrated divergence around a corner of the cubed sphere after a single time step in a pure rotational flow. (top) Analytical and (bottom) numerical formulation of metrics.

unrealistic shortwave oscillations, to which end we follow the method proposed by Sun et al. (1996). In the second step, the conservation is restored following the method described in Sun and Sun (2004).

e. Effect of curvature of coordinates around corners

As a consequence of an increased curvature of the coordinates, we found that a small-scale noise is being generated around corners of the UJ cubed sphere. Initially, we calculated metric terms on a grid with much higher resolution, referring to them as ''analytical metrics.'' An example of the corner noise in the divergence field integrated through all model levels after the first time step in a test with the zonal flow, using this ''analytical'' method is shown in Fig. 5 (top panel).

After replacing analytical with the ''numerical'' metrics, that is, those calculated on the same grid as the finite-differencing schemes, the situation immediately improved, as shown in Fig. 5 (bottom panel), where the amplitude of corner noise is more than one order of magnitude smaller. With the increase of resolution, the amplitude of corner noise gradually decreases, as suggested by Table 1, which shows extreme values of the surface pressure and the horizontal divergence vertically integrated over all levels, respectively, measured around a corner of the cubed sphere for several increasing resolutions (104, 52, and 26 km). Perhaps more importantly, the remaining noise affects significantly the same pattern of only a few grid points clustered around each corner at all resolutions, thus the area affected becomes smaller with the increase of resolution.

To further minimize the effect of corner noise, we additionally apply an inflated divergence damping to the areas around corners:

$$\kappa = \kappa_1 - \kappa_2 \cos x' \cos y' , \qquad (70)$$

where x' and y' are diagonal directions of the cube's face, normalized so that they range from $[-\pi, \pi]$. Coefficients κ_1 and κ_2 are chosen so that minimum damping occurs in the center of the cube and maximum at the corners. This small-scale noise represents a local effect of so-called grid imprinting, that is, an impact of the grid used for discretization on the solution.

6. Test integrations

The model was tested in a series of integrations within the HIWPP project. We here first illustrate model efficiency, and then show two examples of model performance in the idealized tests integrations, and one test case with full physics.

a. Efficiency

In the preliminary tests of model dynamics with the baroclinic test case of Jablonowski and Williamson (2006), the dynamical core of the NMMB-UJ was tested against

TABLE 1. Extreme values of surface pressure (hPa) and vertically integrated horizontal divergence (s^{-1}) around a corner of the cubed sphere.

	$p_{s_{\max}}$	$p_{s_{\min}}$	Δp_s	$\mathrm{Div}_{\max}$	$\mathrm{Div}_{\min}$	$\Delta\mathrm{Div}$
104 km	100 004.02	99 996.02	8	0.033 483 1	−0.033 395 7	0.066 878 8
52 km	100 002.02	99 998.02	4	0.033 149 7	−0.033 198 3	0.066 348
26 km	100 001.02	99 999.02	2	0.033 266 2	−0.032 944 1	0.066 210 3

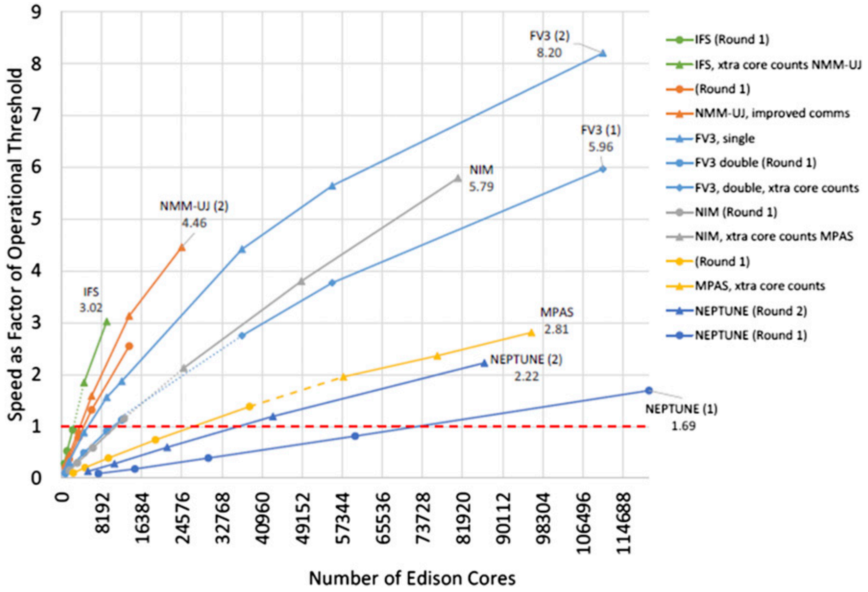

FIG. 6. Scalability of the suite of models in a 3-km test run according to the NGGPS report. Picture shows elapsed time for 30-min simulation using a log–log scale. Lower is better. [Courtesy of Michalakes et al. (2015).]

the original version of the model on the geographical grid. In a 20-day integration on $24 \times 24 \times 6 = 3456$ message passing interface (MPI) processes, using a horizontal resolution of 13 km and 128 vertical levels, and with a time step of 25 s, the cubed-sphere version was 22.57% more efficient than the geographical grid version with polar filtering. Integration of the model on the geographical grid took 4 h, 48 min, and 27 s, while integration of the model on the cubed sphere took 3 h, 43 min, and 20 s. This advantage is expected to become only more pronounced with further increase of resolution and in integrations on larger numbers of processors, because the version on the geographical grid would spend proportionally more time on communication due to the global nature of polar filtering. At the same time, the version running on the cubed sphere would spend proportionally considerably less time on communications. For example, in a test integration at 104 km and 96 MPI processes, NMMB-UJ spent 31% of computing time on communication. When resolution was increased to 3 km and the number of MPI processes to 3456, the relative amount of time for communications dropped to only 8.7%.

Five different global nonhydrostatic gridpoint models participated in test runs of an idealized baroclinic development case used in evaluations of candidate dynamic cores for the National Weather Service's Next Generation Global Prediction System (NGGPS): the Nonhydrostatic Icosahedral Model (NIM) from the NOAA/ESRL, the Model for Prediction Across Scales (MPAS) from NCAR, NEPTUNE from the U.S. Naval Research Laboratory (NRL), FV3 from NOAA/GFDL, and our model, that was referred to as "the uniform-Jacobian version of the Nonhydrostatic Multiscale Model (NMM-UJ) from NOAA/NCEP." The ECMWF's Integrated Forecast System (IFS) was a sixth participant that was included to provide contrast as a spectral (although only hydrostatic) model. Figure 6 from a report by the NGGPS Advanced Computing Evaluation Committee (Michalakes et al. 2015) shows the scaling results of two rounds of runs made of 30-min forecasts with 3-km gridpoint spacing (or its equivalent for IFS) and with 127 or 128 vertical levels (IFS used 137 levels). Forecasts were executed on the Department of Energy's Edison computer at the National Energy Research Scientific Computing in Berkeley, California. Edison is a Cray XC30, with a peak performance of 2.57 petaflops, 133 824 compute cores, 357 terabytes of memory, and 7.56 petabytes of disk. More details about its performance may be found on its website (http://www.nersc.gov/users/computational-systems/edison/). The same forecast was run on processor counts ranging from several thousand to roughly 100 000. The second round was carried out after model developers made various modifications to their systems following round one. Figure 6 shows that the NMMB-UJ had significantly faster run times on the various processor counts compared to the other nonhydrostatic gridpoint models. An early version of the NMMB-UJ dynamic core was used in these tests. Instead of the monotonization and mass restoration

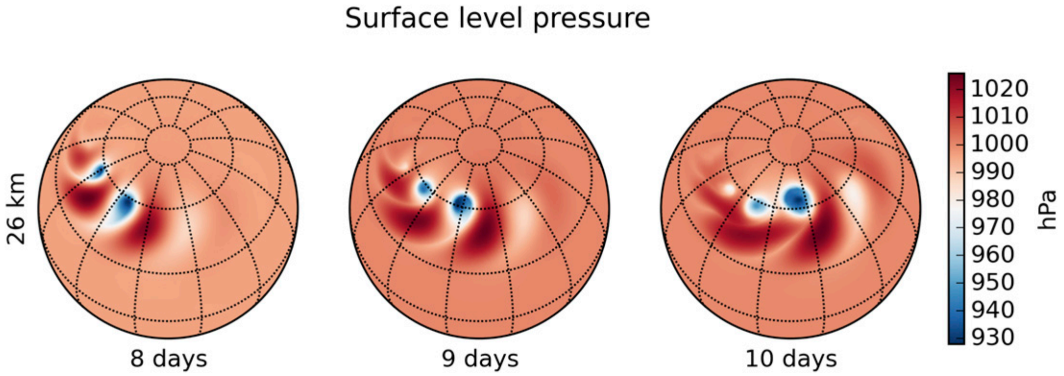

FIG. 7. Evolution of surface level pressure p_s in the baroclinic wave test case at horizontal resolution of 26 km.

algorithms described in section 4e a simpler version currently in use in the original NMMB was in place. Also the second-order version of all horizontal advections schemes was applied.

b. Baroclinic wave

A baroclinic instability test case was suggested in Jablonowski and Williamson (2006). It consists of unstable zonal flow in which a small initial perturbation is applied in the Northern Hemisphere. Precise values of parameters that control this test are taken from Ullrich et al. (2012). We show here tests run at several increasing horizontal resolutions, low (104 km), medium (52 km), and high (26 km), respectively, all with 128 levels. In principle, the horizontal resolution needs to be matched by an appropriately adjusted vertical, as summarized in Iga et al. (2007), but that was not followed in this idealized HIWPP test. The unstable growth is well pronounced at days 8, 9, and 10, as evident from Fig. 7, which shows evolution of surface pressure in the high-resolution test.

Comparing outputs of runs at different resolutions reveals a decent convergence for most of the fields. As an example, we show in Fig. 8 temperature fields at level 100, closest to 850 hPa, at day 9 in tests at all three resolutions.

The difference between runs at different resolutions is best seen in the relative vorticity fields, shown in Fig. 9. Analysis of the model performance at still higher resolutions is presented in Whitaker (2015). With the increase of resolution, our model shows more details of the occlusion, which was absent from the outputs of other models. We speculate that these stripes could be attributed to the capability of our model to correctly describe nonlinear energy cascade, through the Arakawa (1972) principle of integral conservation of kinetic energy and enstrophy, as well as to our constraints on conversion between the kinetic and other forms of energy.

Dry mass, defined as a hydrostatic pressure difference between the top of the model's atmosphere and the surface, is perfectly conserved in this test with variations around 10^{-5} of a percent. Total energy is defined as a sum of kinetic, $(u\tilde{u} + v\tilde{v} + w^2)mG/2$; thermal, $c_p TmG_h$; and potential energy, $gzmG_h$. Evolution of total and kinetic energies normalized by initial values are shown in Fig. 10. Though not visible from the picture, total energy steadily increases by several hundredths of a percent during the first 10 days of integration, which is within the range that could be expected from most models. An increase of kinetic energy in the unstable baroclinic wave development is expected, and is compensated in the overall energy budget by the imposed conservation constraints.

The baroclinic wave test case also revealed a large-scale effect of grid imprinting, that is, a grid-biased balanced solution that on the cubed sphere is less natural than on the longitude–latitude grid (e.g., Janjić and Vasic 2015). Figure 11 shows surface pressure in the Southern Hemisphere in the baroclinic test case after 17 days of integration at the low resolution, which clearly reveals the effect of the cubed-sphere geometry on the solution. Similar patterns were present in outputs of all other models that used quasi-uniform grids within the HIWPP project, but not in the output of the NMMB running on the geographical grid.

c. Supercell thunderstorm

The second idealized test is a supercell thunderstorm on a reduced-radius sphere without rotation, with parameters as described in, for example, Klemp et al. (2015).

This test starts from conditionally unstable initial conditions, characterized by a large value of convective available potential energy (CAPE) and a strong low-level wind shear, which is critical for the creation of supercell activity. For this test case the model used a

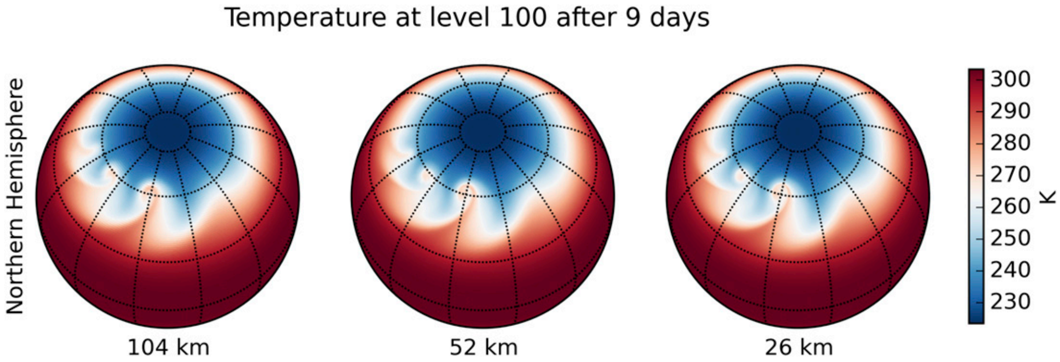

FIG. 8. Temperature field at level 100 after 9 days in the baroclinic wave test case at three different resolutions: (from left to right) 104, 52, and 26 km.

simple warm-rain Kessler-type microphysics (Kessler 1969), necessary for explicit treatment of moist convection. A coefficient of linear horizontal and vertical diffusion is prescribed in order to provide correct convergence of the solution across different scales.

In our case, the initial conditions were inherited from the global NMMB on the geographical grid and then interpolated to the cubed sphere, which produced an initial background noise that compounded with the effects of grid imprinting, and required somewhat larger initial divergence damping to keep it under control.

Four tests were run at increasing resolutions of 4, 2, 1, and 0.5 km on the reduced sphere. Figure 12 shows the vertical winds at the level closest to 2.5 km after 90 min, which closely corresponds to figures shown in the HIWPP report of Whitaker (2015). For brevity, only tests run at 1° and 0.5° are presented. Figure 13 shows diagnostics of maximum wind and total rain in tests at all resolutions. The position and magnitude of the derived vertical wind field generally agree with those of other groups, with admittedly somewhat slower separation and rotation of the convective cells, which is the result of inflated divergence damping and appears to be completely unrelated to the treatment of nonhydrostatic effects.

d. 3-km test run with full physics

Within the HIWPP project another test was that which included the Moore tornado case of 20 May 2013 (e.g., Atkins et al. 2014). The forecast was run to 72 h with gridpoint spacing of 3 km. The physics used by the NMMB-UJ was taken from the global NMMB on the geographic grid. The main features of both physics are summarized in Table 2.

The initial time of the forecast was 0000 UTC 18 May 2013. A fundamental question is whether the forecast could produce any indication of the squall line near the end of the forecast period when it actually occurred in nature. The tornado itself touched down at 1956 UTC 20 May and was on the ground for 39 min. The top panel of Fig. 14 shows the observed radar reflectivity at 2100 UTC 20 May less than an hour after the storm hit. The bottom panel depicts

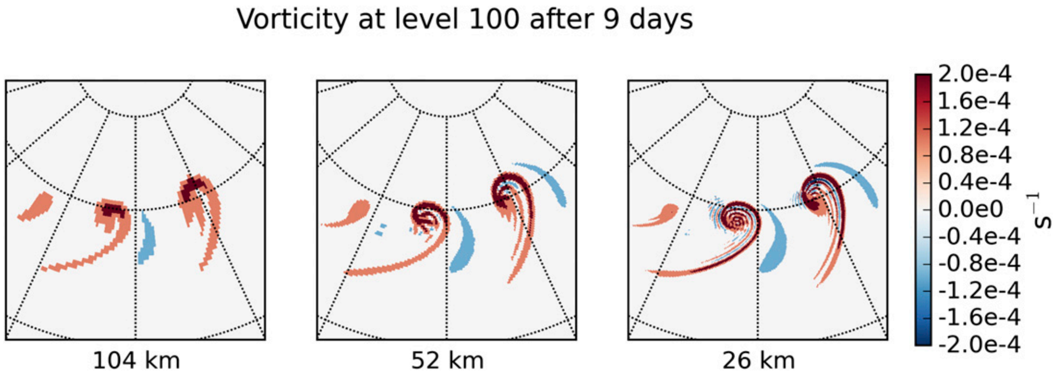

FIG. 9. Relative vorticity at level 100 after 9 days in the baroclinic wave test case at three different resolutions: (from left to right) 104, 52, and 26 km.

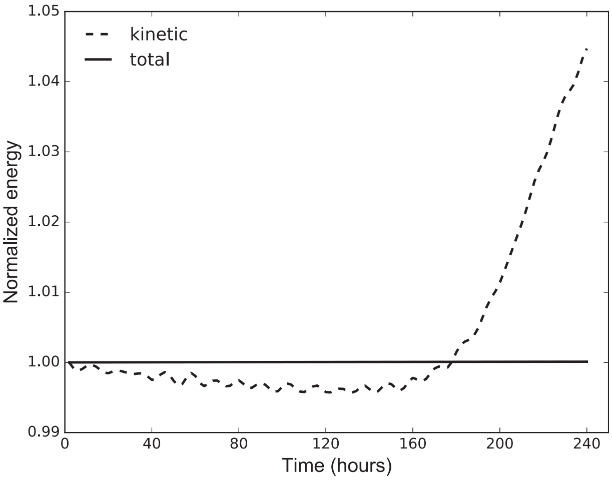

FIG. 10. Evolution of total and kinetic energy in the baroclinic wave test case.

the NMMB-UJ forecast for cloud condensate at 2200 UTC in a model layer near the middle of the atmosphere. The forecast cloud field indicates that a line did develop very near the proper location 70 h into the forecast, or about 1 h later than observed. This shows that in this case the NMMB-UJ with this physics package was able to predict at least certain aspects of a significant severe weather event with considerable accuracy.

7. Conclusions

In this paper we describe transfer of the NMMB, a second-order, finite-differencing global model of the atmosphere based on strict enforcement of mimetic properties, to a novel UJ cubed-sphere grid geometry. The UJ cubed sphere exploits assumptions of uniform Jacobians, minimizing the difference between the smallest and longest grid distance, and perfectly preserving smoothness of the coordinate lines. For brevity, we here show only results of two idealized test cases proposed within HIWPP (i.e., the unstable baroclinic wave and supercell thunderstorm test cases). The results of nonhydrostatic orographic mountain waves test cases will be shown elsewhere. In general, we were able to reconstruct the idealized test solutions proposed by HIWPP and to produce a high-resolution forecast with full physics coinciding with a significant weather event while demonstrating excellent computational performance.

To fully understand why the computational performance of NMMB-UJ was better than that of other participating models would require an in depth analysis, which is outside the scope of this paper. We speculate that the model design and chosen numerical grid both helped in that respect:

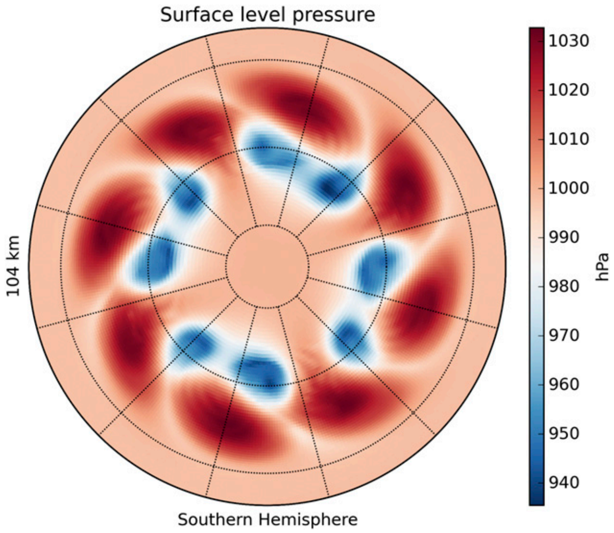

FIG. 11. Surface level pressure on Southern Hemisphere in the baroclinic instability test case at 104 km after 17 days of integration.

- The NMMB model is a straightforward second-order model, and with the exception of the new monotonization filter that was added at a later stage, the model almost completely eliminates global interprocessor communications, which explains its good scaling.
- NMMB has a unique, extremely efficient treatment of nonhydrostatic effects, which allows it to solve two fewer prognostic equations than other models.
- Vertical advections are solved in an efficient implicit way.
- Topology of the cubed sphere is convenient for parallelization.
- UJ mesh allows use of a sufficiently large time step.

The UJ cubed sphere with its smoothness and homogeneity offers an excellent computational paradigm. However, we found that just as with other spherical polyhedral grids the main issue of concern is grid imprinting.

The local manifestation of that problem is the generation of small scale noise around corners of the UJ cubed sphere, which is presumably a consequence of the increased curvature of the coordinate lines. Perhaps it could be explained by a local loss of numerical accuracy (e.g., Peixoto and Barros 2013). In this paper, we deal with the corner noise using a locally inflated divergence damping. In addition, we have found that when the formulation of grid metrics is done

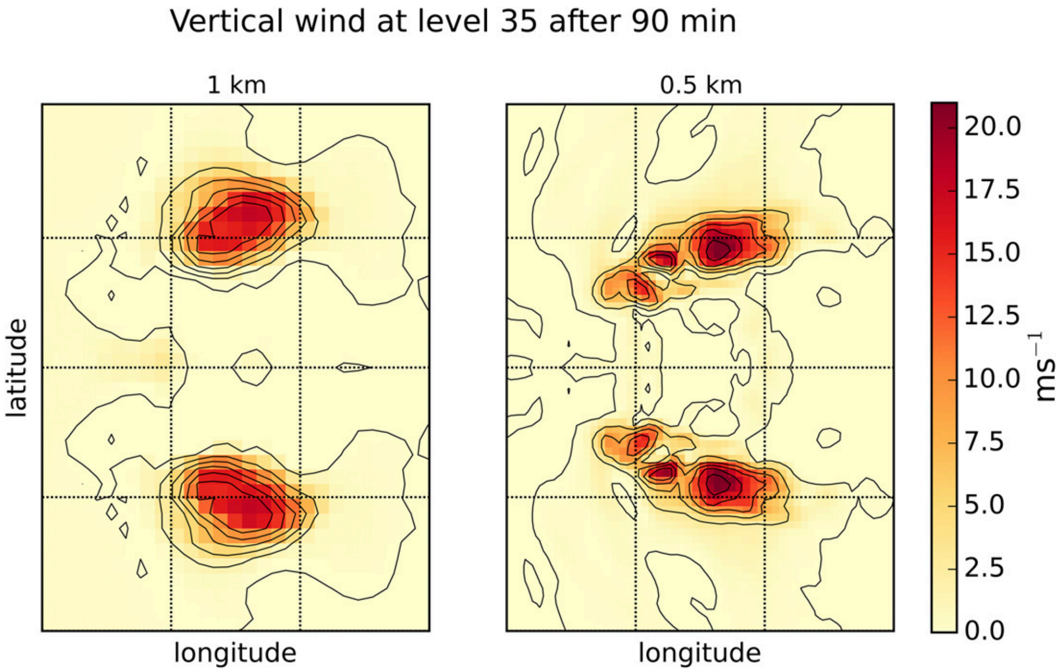

FIG. 12. Vertical wind in the idealized supercell thunderstorm test case at resolutions of (left) 1 km and (right) 0.5 km after 90 min of integration at level 35 closest to 2.5 km.

consistently with model discretization, the noise observed during the first time step in the baroclinic wave test case quickly disappears. The most seriously affected was the idealized test on the reduced sphere, where the divergent portion of the flow is dominant over planetary scales, a situation that the underlying philosophy of our model is not well suited to deal with. We are still looking for a more effective remedy of the corner noise on the UJ cubed sphere, and the results will be discussed elsewhere. Still, as one can expect, this issue becomes less significant with the increase of horizontal resolution, and while running the model at 3 km with full physics the corner noise had no visible effect over the first 72 h of integration that we were performing.

Another manifestation of the grid imprinting is a grid bias observed at large scales of the balanced solution, revealed in the long-term integrations without physical forcing, which could be ascribed to the stationary geostrophic modes according to Weller et al. (2012).

It is possible that models using finite-volume methods (e.g., Lin 2004; Li et al. 2013; Smolarkiewicz et al. 2014), because of their inherent application of monotonization limiters, or those based on spectral elements (e.g., Wang et al. 2007; Evans et al. 2013; Giraldo et al. 2013), including discontinuous Galerkin methods (e.g., Bao et al. 2015), because of their ability to locally increase accuracy, are better equipped to deal with the noise around singular points on quasi-uniform grids. However, all models that participated in HIWPP, with the exception of NMMB on the longitude–latitude grid, showed signs of grid imprinting on the large scales in the long-term integrations (Whitaker 2015; Janjić and Vasic 2015). Thus, one should be vigilant in climate simulations

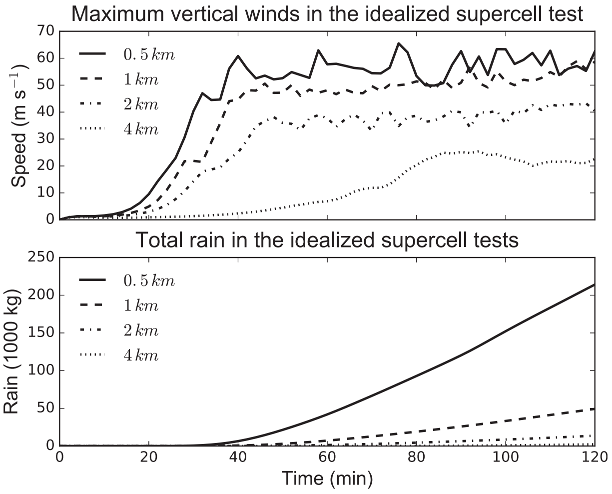

FIG. 13. Diagnostics in the idealized supercell thunderstorm test cases: (top) maximum vertical winds and (bottom) total rain.

TABLE 2. Physics used in NMMB-UJ.

Package	References
Ferrier–Aligo microphysics	Ferrier et al. (2002, 2011), Aligo et al. (2014)
Noah land surface	Ek et al. (2003)
Mellor–Yamada–Janjić turbulence	Mellor and Yamada (1974), Janjić (1990)
Betts–Miller–Janjić convection	Betts and Miller (1986), Janjić (1994)
RRTMG radiation	Iacono et al. (2008)

with such models since physics alone may not be sufficient to prevent spurious forcing (even if only at relatively low amplitudes) of patterns locked in phase with the grid.

The Janjić unique method for treatment of nonhydrostatic effects is often misunderstood because it avoids solving two prognostic equations, for the vertical wind and the pressure. Actually, in the framework of approach postulated by Laprise (1992), the hydrostatic mass m is analogous to density in the system with geometrical height as the vertical coordinate. Solving prognostic equations for hydrostatic mass m and temperature T eliminates the need to solve the prognostic equation for pressure. The only slight glitch that we were able to find with this approach is that all variables on the right-hand side of the hydrostatic relation (28) are not defined at the same time level, suggesting that further analysis may be beneficial. Nevertheless, Janjić et al. (2001) found a method that efficiently and correctly adds the nonhydrostatic effects to a preexisting hydrostatic framework.

In some future updates, additional conservation constraints could be added to the vertical discretization (e.g., Juang 2011), and the model may benefit from an increased order of accuracy in the vertical direction (e.g., Ullrich and Guerra 2015). Finally, an approximately regular version of double-sided (''dihedron'') octagonal grid (Purser and Rančić 1997), may undergo the same Jacobian-homogenization procedure as the UJ cubic grid. The resulting ''UJ octagonal grid'' would also offer an attractive computational paradigm. With singularities removed from midlatitudes where the baroclinic instabilities dominate, two large uniform domains convenient for nesting and with potentially more options for parallelization, such a grid would be also of interest for operations on tens of thousands of processors.

Still, the grid geometry of the cubed sphere possesses a remarkable symmetry, and the UJ homogenization provides good computational efficiency by enabling use of time step close to that of the equiangular gnomonic cubed sphere but with a smooth transition across the edges, making this approach very attractive for numerical modeling of geophysical fluids.

Acknowledgments. The described research was accomplished within the High Impact Weather Prediction Project (HIWPP) Non-Hydrostatic (7000P) program, funded by Hurricane Sandy Disaster Relief Supplemental Appropriations Act of 2013 (P.L. 113-2). Many elements of the algorithmic and computing infrastructure were developed within two National Science Foundation grants (ATM-0739518 and ATM-0113037). We would also like to express our gratitude to Drs. Hilary Weller, Lucas Harris, and two other unknown reviewers of our paper for their helpful and constructive comments. Special thanks to the NOAA's Senior Adviser for Advanced Modeling, Dr. Hendrik Tolman; the Director of EMC, Dr. Mike Farrar; and the Chief of EMC's Mesoscale Modeling Branch, Dr. Geoff DiMego, for their continuous support.

APPENDIX

Conservation of Mass and Kinetic Energy

Since the corners represent singular points prone to violating conservation properties of the numerical schemes, we will here explain how the conservation of mass and kinetic energy is accomplished in the NMMB on the UJ cubed sphere. This discussion has nothing to do with the observed grid imprinting, which is prevailingly a consequence of adjustment terms.

We will first consider conservation of mass by the finite-differencing continuity equation (43), and to this end, we use stencils in Figs. A1. Equation (43) has to be modified at the corner points where geometry from the rest of the domain breaks. To guarantee cancellation of all fluxes after global summation, we can, for example, write the continuity equation at the corner point in Fig. A1 as

$$\frac{\partial m}{\partial t} = -\frac{1}{G_c}\left[\frac{2}{3}\frac{1}{d}\left(U_{1/2} - V_{1/3} + \langle V_{2/3} \quad (\mathrm{or}) - U_{2/3}\rangle\right) + \frac{1}{3}\frac{1}{d\sqrt{2}}\left(U'_2 - U'_3 \quad - V'_1\right)\right]. \tag{A1}$$

The notation assumes the northwest corner of the shaded domain that belongs to the cube's face I in Fig. A1, with (x, y) and (x', y') directions defined with

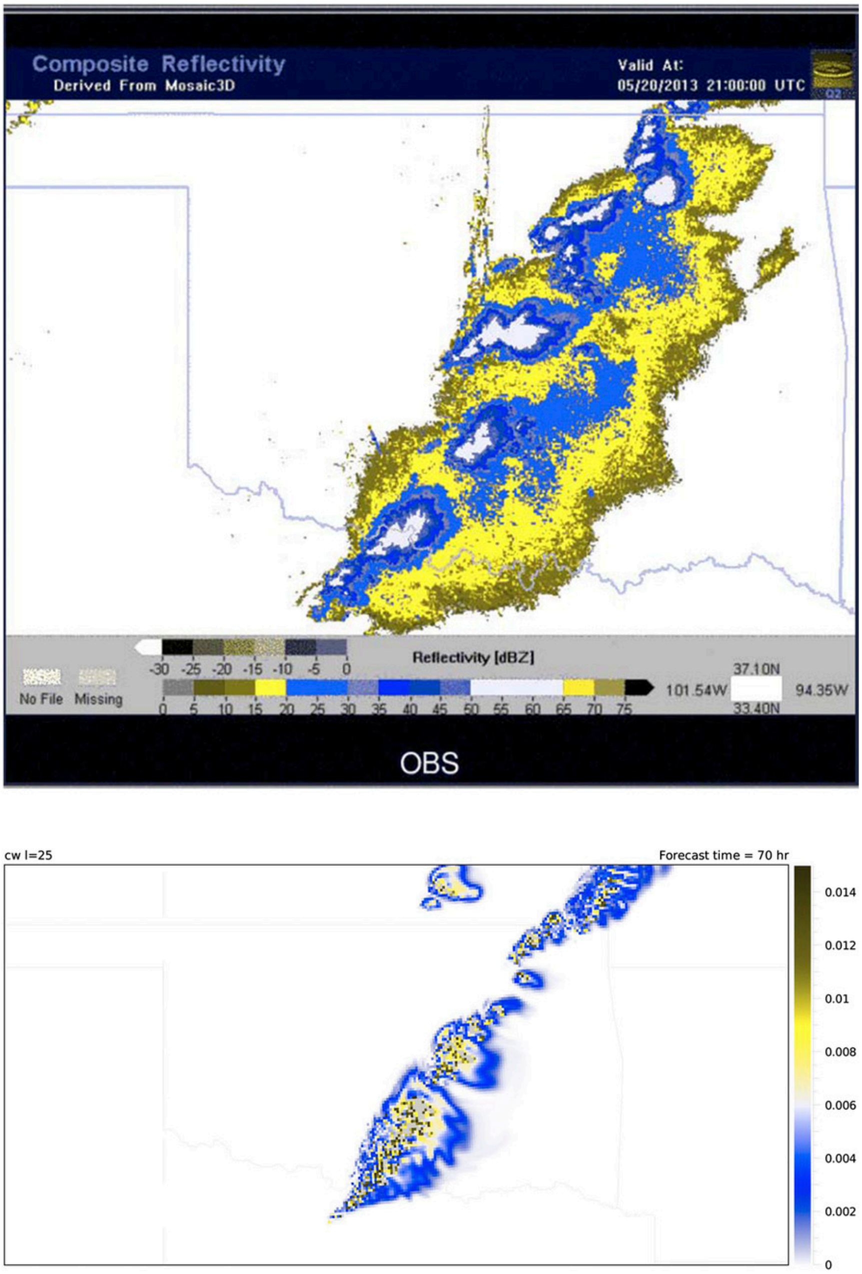

FIG. 14. (top) Radar reflectivity at 2100 UTC 20 May 2013 over Moore, OK. (bottom) Forecast of cloud condensate at model level 25 out of 58 levels, after 70 h of forecast for 2200 UTC.

respect to that face. The normal flux in the angle bracket could be referred to as either $U_{2/3}$ or $V_{2/3}$, depending on if we assume that it belongs to the face II or to the face III. Here G_c denotes the Jacobian at the corner point, which on the UJ cubed sphere we define as $3/4G$. A good way to generalize such a clumsy corner notation, is to introduce a ''ghost space'' (Fig. A1b) and assume that the ghost wind is equal to zero, that is, $\mathbf{v}_G = 0$. Such an approach returns order into the finite-differencing world, but now the normal fluxes $V_{2/3}$ and $-U_{2/3}$ are replaced by their ''partial'' versions, $V^p_{2/3}$ and $-U^p_{2/3}$, where the sum of partial fluxes gives the real flux, that is,

$$U_{2/3} = \frac{1}{4}(\tilde{u}_3 - \tilde{v}_2)(h_0 + h_{2/3}),$$

$$V_{2/3} = \frac{1}{4}(\tilde{v}_2 - \tilde{u}_3)(h_0 + h_{2/3}). \qquad \text{(A2)}$$

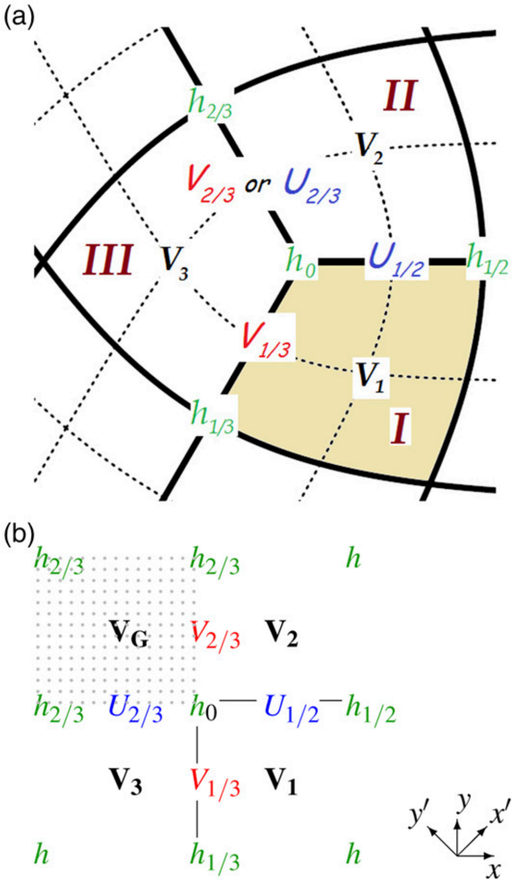

FIG. A1. Stencils to aid explanation of mass conservation strategy. (a) Physical space around a corner point. (b) Computational interpretation of this physical space.

$$U^p_{2/3} = \frac{1}{4}(\tilde{u}_3 + \tilde{u}_G)(h_0 + h_{2/3}),$$

$$V^p_{2/3} = \frac{1}{4}(\tilde{v}_2 + \tilde{v}_G)(h_0 + h_{2/3}), \tag{A3}$$

and, therefore,

$$V^p_{2/3} - U^p_{2/3} = V_{2/3} = -U_{2/3}. \tag{A4}$$

Now the continuity equation (43) is applicable at the corners, or, written explicitly,

$$\frac{\partial m}{\partial t} = -\frac{1}{G_c}\left[\frac{2}{3}\frac{1}{d}(U_{1/2} - U^p_{2/3} + V^p_{2/3} - V_{1/3}) + \frac{1}{3}\frac{1}{d\sqrt{2}}(U'_2 - U'_3 + V'_G - V'_1)\right], \tag{A5}$$

but we should bear in mind when calculating close to the corners, that the fluxes along boundaries between two other faces are only partial proxies, not the real, full fluxes.

The concept of partial fluxes is also used to provide the correct transformation between available potential and kinetic energy in (50) and to ensure the conservation of scalars in (69) during horizontal advection. In the latter case, for example, (69) is multiplied by *Gm* and combined with the continuity equation (43). After applying the following rule:

$$\overline{A\delta_s\psi}^s = \delta_s(\psi\overline{A}^s) - \psi\delta_s A, \tag{A6}$$

we get the following expression for the mass of scalar ψ:

$$\frac{(\partial Gm\psi)}{\partial t} = -\frac{2}{3}[\delta_x(\psi\overline{U}^x) + \delta_y(\psi\overline{V}^y)] - \frac{1}{3}[\delta_{x'}(\psi\overline{U'}^{x'}) + \delta_{y'}(\psi\overline{V'}^{y'})]. \tag{A7}$$

Using consistently ghost space zeros for the definition of ghost space diagonal and partial normal fluxes will provide cancellation of all terms in a global summation.

To get the tendency of kinetic energy, we multiply (53) by $\overline{hG}^{xy}\mathbf{V}$, and apply the finite-differencing rule:

$$u\overline{A\delta_s u}^s = \delta_s\left(A\frac{1}{2}\widetilde{uu}^s\right) - \frac{u^2}{2}\delta_s A, \tag{A8}$$

where $\widetilde{uu}^s$ denotes the product of two neighboring values of a variable u arranged along the coordinate s. The resulting expression reads as follows:

$$\frac{\partial(\overline{hG}^{xy}\mathbf{v}^2/2)}{\partial t} = \frac{\mathbf{v}^2}{2}\frac{\partial\overline{hG}^{xy}}{\partial t} - \frac{2}{3}\left[\delta_x\left(\mathscr{U}\frac{1}{2}\widetilde{\mathbf{vv}}^x\right) + \delta_y\left(\mathscr{V}\frac{1}{2}\widetilde{\mathbf{vv}}^y\right)\right] + \frac{1}{3}\left[\delta_{x'}\left(\mathscr{U}'\frac{1}{2}\widetilde{\mathbf{vv}}^{x'}\right) + \delta_{y'}\left(\mathscr{V}'\frac{1}{2}\widetilde{\mathbf{vv}}^{y'}\right)\right] + \frac{\mathbf{v}^2}{2}\left[\frac{2}{3}\left(\delta_x\mathscr{U} + \delta_y\mathscr{V}\right) + \frac{1}{3}\left(\delta_{x'}\mathscr{U}' + \delta_{y'}\mathscr{V}'\right)\right]. \tag{A9}$$

Terms in the second row in the first two square brackets of (A9) are written in flux form and should not contribute to the generation of kinetic energy after global summation, because they will all cancel among themselves. However, two important observations should be made. First, the mass fluxes $\mathscr{U}$ and

$\mathscr{V}'$ in this equation cannot involve partial, but only full fluxes U and V. Second, the flux of kinetic energy going directly onto the corner (flux $\mathscr{V}'(1/2)\widetilde{\mathbf{v}\mathbf{v}}^{y'}$ in Fig. A1) will cancel *regardless of the definition of flux* $\mathscr{V}'$, because one of the winds in the product is the zero-wind from the ‘‘ghost’’ space. That gives us some space for maneuvering as will become clear below.

The first term on the right-hand side of (A9) should cancel the last term in the square bracket in order to prevent spurious generation of kinetic energy. That is indeed satisfied everywhere in the domain, with the exception of wind points in the corners of the cube's faces (point $\mathbf{v}_1$ on Fig. A1), because the first term includes the continuity equation applied at the corners, which involves ‘‘partial’’ fluxes, and the last term is made exclusively from full fluxes.

One way to provide cancellation of these two terms is through definition of the diagonal flux V'_G, which is included in definition of flux $\mathscr{V}'$ through averaging in (55). By recalling that the continuity equation uses partial fluxes and assumes that the diagonal flux in the ghost space is zero, we get the following relation for the definition of diagonal ghost flux in the momentum equation:

$$\frac{2}{3}\frac{1}{d}(-U^p_{2/3} + V^p_{2/3}) = \frac{2}{3}\frac{1}{d}(-U_{2/3} + V_{2/3}) + \frac{1}{3}\frac{1}{d\sqrt{2}}V'_G. \tag{A10}$$

By taking into account (A4) we get

$$V'_G = 2\sqrt{2}U_{2/3} = -2\sqrt{2}V_{2/3}. \tag{A11}$$

Conservation of the second moment of scalar ψ can be verified if (A7) is multiplied once again by ψ, and then by applying the rule (A8), with u replaced by ψ. The rules in (A6), (A8), and a series of similar convenient formulas for manipulations of finite differences are collected in Gavrilov et al. (2014).

We should mention that momentum is not conserved by the pressure gradient force at the corners. Also, we do not use a curvilinear analogy of the Janjić (1984) nonlinear momentum advection scheme that, by conserving the C-grid version of enstrophy on the semistaggered grid, could further improve the simulation of the nonlinear energy cascade. Implementation of that scheme in the framework of quasi-uniform grids still remains to be accomplished.

REFERENCES

Aligo, E., B. Ferrier, J. Carley, M. Pyle, D. Jovic, and G. DiMego, 2014: High-resolution NMMB simulation of the 29 June 2012 derecho. *26th Conf. on Weather Analysis and Forecasting/22nd Conf. on Numerical Weather Prediction*, Atlanta, GA, Amer. Meteor. Soc., 14.4. [Available online at https://ams.confex.com/ams/94Annual/webprogram/Paper238154.html.]

Arakawa, A., 1966: Computational design for long-term numerical integration of the equations of fluid motion: Two-dimensional incompressible flow. Part I. *J. Comput. Phys.*, **1**, 119–143, doi:10.1016/0021-9991(66)90015-5.

——, 1972: Design of the UCLA general circulation model. Tech. Rep. 7, Department of Meteorology, University of California, Los Angeles, 116 pp.

——, and V. Lamb, 1977: Computational design of the basic dynamical processes of the UCLA general circulation model. *Methods in Computational Physics: Advances in Research and Applications*, J. Chang, Ed., Academic Press, 173–265.

Atkins, N. T., K. M. Butler, K. R. Flynn, and R. M. Wakimoto, 2014: An integrated damage, visual, and radar analysis of the 2013 Moore, Oklahoma, EF5 tornado. *Bull. Amer. Meteor. Soc.*, **95**, 1549–1561, doi:10.1175/BAMS-D-14-00033.1.

Bao, L., R. Klöfkorn, and R. D. Nair, 2015: Horizontally explicit and vertically implicit (HEVI) time discretization scheme for a discontinuous Galerkin nonhydrostatic model. *Mon. Wea. Rev.*, **143**, 972–990, doi:10.1175/MWR-D-14-00083.1.

Betts, A., and M. Miller, 1986: A new convective adjustment scheme. Part II: Single column tests using GATE wave, BOMEX, ATEX and arctic air-mass data sets. *Quart. J. Roy. Meteor. Soc.*, **112**, 693–709, doi:10.1002/qj.49711247308.

Eckermann, S., 2009: Hybrid σ–p coordinate choices for a global model. *Mon. Wea. Rev.*, **137**, 224–245, doi:10.1175/2008MWR2537.1.

Ek, M. B., K. Mitchell, Y. Lin, E. Rogers, P. Grunmann, V. Koren, G. Gayno, and J. Tarpley, 2003: Implementation of Noah land surface model advances in the National Centers for Environmental Prediction operational mesoscale Eta model. *J. Geophys. Res.*, **108**, 8851, doi:10.1029/2002JD003296.

Evans, K., P. Lauritzen, S. Mishra, R. Neale, M. Taylor, and J. Tribbia, 2013: AMIP simulation with the CAM4 spectral element dynamical core. *J. Climate*, **26**, 689–709, doi:10.1175/JCLI-D-11-00448.1.

Ferrier, B., Y. Jin, Y. Lin, T. Black, E. Rogers, and G. DiMego, 2002: Implementation of a new grid-scale cloud and precipitation scheme in the NCEP Eta model. Preprints, *15th Conf. on Numerical Weather Prediction*, San Antonio, TX, Amer. Meteor. Soc., 280–283.

——, W. Wang, and E. Colón, 2011: Evaluating cloud microphysics schemes in nested NMMB forecasts. *24th Conf. on Weather Analysis and Forecasting/20th Conf. on Numerical Weather Prediction*, Seattle, WA, Amer. Meteor. Soc., 14B.1. [Available online at https://ams.confex.com/ams/91Annual/webprogram/Paper179488.html.]

Gavrilov, B., I. Tošić, and M. Rančić, 2014: *Numerical Methods in Meteorology: Solved Problems*. Lap Lambert Academic Publishing, 172 pp.

Giraldo, F., J. Kelly, and E. Constantinescu, 2013: Implicit-explicit formulations of a three-dimensional nonhydrostatic unified model of the atmosphere (NUMA). *SIAM J. Sci. Comput.*, **35**, B1162–B1194, doi:10.1137/120876034.

Iacono, M. J., J. S. Delamere, E. J. Mlawer, M. W. Shephard, S. A. Clough, and W. D. Collins, 2008: Radiative forcing by long-lived greenhouse gases: Calculations with the AER radiative transfer models. *J. Geophys. Res.*, **113**, D13103, doi:10.1029/2008JD009944.

Iga, S., H. Tomita, M. Satoh, and K. Goto, 2007: Mountain-wave-like spurious waves associated with similated cold fronts due to inconsistencies between horizontal and vertical resolutions. *Mon. Wea. Rev.*, **135**, 2629–2641, doi:10.1175/MWR3423.1.

Jablonowski, C., and D. Williamson, 2006: A baroclinic instability test case for atmospheric model dynamic cores. *Quart. J. Roy. Meteor. Soc.*, **132**, 2943–2975, doi:10.1256/qj.06.12.

Janjić, Z., 1974: A stable centered difference scheme free of two-grid-interval noise. *Mon. Wea. Rev.*, **102**, 319–323, doi:10.1175/1520-0493(1974)102<0319:ASCDSF>2.0.CO;2.

——, 1984: Nonlinear advection schemes and energy cascade on semi-staggered grids. *Mon. Wea. Rev.*, **112**, 1234–1245, doi:10.1175/1520-0493(1984)112<1234:NASAEC>2.0.CO;2.

——, 1990: The step-mountain coordinate: Physical package. *Mon. Wea. Rev.*, **118**, 1429–1443, doi:10.1175/1520-0493(1990)118<1429:TSMCPP>2.0.CO;2.

——, 1994: The step-mountain eta coordinate model: Further developments of the convection, viscous sublayer, and turbulence closure schemes. *Mon. Wea. Rev.*, **122**, 927–945, doi:10.1175/1520-0493(1994)122<0927:TSMECM>2.0.CO;2.

——, 2003: A nonhydrostatic model based on a new approach. *Meteor. Atmos. Phys.*, **82**, 271–301, doi:10.1007/s00703-001-0587-6.

——, and R. Gall, 2012: Scientific documentation of the NCEP nonhydrostatic multiscale model on the B grid (NMMB). Part 1: Dynamics. NCAR Tech. Note, NCAR/TN-489+STR, 75 pp., doi:10.5065/D6WH2MZX.

——, and R. Vasic, 2015: Challenges and opportunities in modeling of the global atmosphere. *27th Conf. on Weather Analysis and Forecasting/23rd Conf. on Numerical Weather Prediction*, San Antonio, TX, Amer. Meteor. Soc., 4A.3. [Available online at https://ams.confex.com/ams/27WAF23NWP/webprogram/Paper273471.html.]

——, J. Gerrity, and S. Nickovic, 2001: An alternative approach to nonhydrostatic modeling. *Mon. Wea. Rev.*, **129**, 1164–1178, doi:10.1175/1520-0493(2001)129<1164:AAATNM>2.0.CO;2.

——, T. Janjić, and R. Vasic, 2011: A class of conservative fourth-order schemes and impact of enhanced formal accuracy on extended-range forecast. *Mon. Wea. Rev.*, **139**, 1556–1568, doi:10.1175/2010MWR3448.1.

Juang, H.-M. H., 2011: A multiconserving discretization with enthalpy as a thermodynamic prognostic variable in generalized hybrid vertical coordinates for the NCEP global forecast system. *Mon. Wea. Rev.*, **139**, 1583–1607, doi:10.1175/2010MWR3295.1.

Kasahara, A., 1974: Various vertical coordinate systems used in numerical weather prediction. *Mon. Wea. Rev.*, **102**, 509–522, doi:10.1175/1520-0493(1974)102<0509:VVCSUF>2.0.CO;2.

Kessler, E., 1969: *On the Distribution and Continuity of Water Substance in Atmospheric Circulation*. *Meteor. Monogr.*, No. 32, Amer. Meteor. Soc., 88 pp.

Klemp, J., W. Skamarock, and S.-H. Park, 2015: Idealized global nonhydrostatic atmospheric test cases on a reduced-radius sphere. *J. Adv. Model. Earth Syst.*, **7**, 1155–1177, doi:10.1002/2015MS000435.

Laprise, R., 1992: The Euler equations of motion with hydrostatic pressure as an independent variable. *Mon. Wea. Rev.*, **120**, 197–207, doi:10.1175/1520-0493(1992)120<0197:TEEOMW>2.0.CO;2.

Li, X., C. Chen, X. Shen, and F. Xiao, 2013: A multimoment constrained finite-volume model for nonhydrostatic atmospheric dynamics. *Mon. Wea. Rev.*, **141**, 1216–1240, doi:10.1175/MWR-D-12-00144.1.

Lin, S.-J., 2004: A "vertically Lagrangian" finite volume dynamical core for global models. *Mon. Wea. Rev.*, **132**, 2293–2307, doi:10.1175/1520-0493(2004)132<2293:AVLFDC>2.0.CO;2.

Lorenz, E. N., 1960: Energy and numerical weather prediction. *Tellus*, **12A**, 364–373, doi:10.1111/j.2153-3490.1960.tb01323.x.

Lovelock, D., and H. Rund, 1975: *Tensors, Differential Forms, and Variational Principles*. John Wiley and Sons, 366 pp.

McGregor, L., 1996: Semi-Lagrangian advection on conformal-cubic grids. *Mon. Wea. Rev.*, **124**, 1311–1322, doi:10.1175/1520-0493(1996)124<1311:SLAOCC>2.0.CO;2.

Mellor, G., and T. Yamada, 1974: A hierarchy of turbulence closure models for planetary boundary layers. *J. Atmos. Sci.*, **31**, 1791–1806, doi:10.1175/1520-0469(1974)031<1791:AHOTCM>2.0.CO;2.

Mesinger, F., 1973: A method for construction of second-order accuracy difference schemes permitting no false two-grid-interval wave in the height field. *Tellus*, **25A**, 444–458, doi:10.1111/j.2153-3490.1973.tb00629.x.

Michalakes, J., and Coauthors, 2015: AVEC Report: NGGPS level-1 benchmarks and software evaluation. Advanced Computing Evaluation Committee, 22 pp. [Available at https://www.earthsystemcog.org/site_media/projects/dycore_test_group/20150602_AVEC_Level_1_Benchmarking_Report_08.pdf.]

Peixoto, P. S., and R. M. Barros, 2013: Analysis of grid imprinting on geodesic spherical icosahedral grids. *J. Comput. Phys.*, **237**, 61–78, doi:10.1016/j.jcp.2012.11.041.

Purser, R. J., 1988: Degradation of numerical differencing caused by Fourier filtering at high latitudes. *Mon. Wea. Rev.*, **116**, 1057–1066, doi:10.1175/1520-0493(1988)116<1057:DONDCB>2.0.CO;2.

——, and M. Rančić, 1997: Conformal octagon: An attractive framework for global models offering quasi-uniform regional enhancement of resolution. *Meteor. Atmos. Phys.*, **62**, 33–48, doi:10.1007/BF01037478.

——, and ——, 1998: Smooth quasi-homogeneous gridding of the sphere. *Quart. J. Roy. Meteor. Soc.*, **124**, 637–647, doi:10.1002/qj.49712454612.

——, and ——, 2011: A standardized procedure for the derivation of smooth and partially overset grids on the sphere, associated with polyhedra that admit regular griddings of their surfaces. Part I: Mathematical principles of classification and construction. NOAA/NCEP Office Note 467, 56 pp. [Available at http://www.emc.ncep.noaa.gov/officenotes/FullTOC.html.]

Rančić, M., R. J. Purser, and F. Mesinger, 1996: A global shallow-water model using an expanded spherical cube: Gnomonic versus conformal coordinates. *Quart. J. Roy. Meteor. Soc.*, **122**, 959–982, doi:10.1002/qj.49712253209.

——, H. Zhang, and V. Savic-Jovcic, 2008: Nonlinear advection schemes on the octagonal grid. *Mon. Wea. Rev.*, **136**, 4668–4686, doi:10.1175/2008MWR2477.1.

Randall, D., and Coauthors, 1998: Status of and outlook for large-scale modeling of atmosphere–ice–ocean interactions in the Arctic *Bull. Amer. Meteor. Soc.*, **79**, 197–219, doi:10.1175/1520-0477(1998)079<0197:SOAOFL>2.0.CO;2.

Ronchi, C., R. Iacono, and R. Paolucci, 1996: The "cubed sphere": A new method for the solution of partial differential equations in spherical geometry. *J. Comput. Phys.*, **124**, 93–114, doi:10.1006/jcph.1996.0047.

Sadourny, R., 1972: Conservative finite-difference approximations of the primitive equations on quasi-uniform spherical grids. *Mon. Wea. Rev.*, **100**, 136–144, doi:10.1175/1520-0493(1972)100<0136:CFAOTP>2.3.CO;2.

Smagorinsky, J., 1963: General circulation experiments with the primitive equations. 1. The basic experiment. *Mon. Wea. Rev.*, **91**, 99–164, doi:10.1175/1520-0493(1963)091<0099:GCEWTP>2.3.CO;2.

Smolarkiewicz, P., C. Kühnlein, and N. Wedi, 2014: A consistent framework for discrete integrations of soundproof and compressible PDEs of atmospheric dynamics. *J. Comput. Phys.*, **263**, 185–205, doi:10.1016/j.jcp.2014.01.031.

Sun, W.-Y., and M.-T. Sun, 2004: Mass correction applied to semi-Lagrangian advection scheme. *Mon. Wea. Rev.*, **132**, 975–984, doi:10.1175/1520-0493(2004)132<0975:MCATSA>2.0.CO;2.

——, K.-S. Yeh, and R.-Y. Sun, 1996: A simple semi-Lagrangian scheme for advection equations. *Quart. J. Roy. Meteor. Soc.*, **122**, 1211–1226, doi:10.1002/qj.49712253310.

Synge, J. L., and A. Schild, 1949: *Tensor Calculus*. University of Toronto, 324 pp.

Takacs, L., and R. Balgovind, 1983: High latitude filtering in global grid point models. *Mon. Wea. Rev.*, **111**, 2005–2015, doi:10.1175/1520-0493(1983)111<2005:HLFIGG>2.0.CO;2.

Tomita, H., M. Tsugawa, M. Satoh, and K. Goto, 2001: Shallow water model on a modified icosahedral geodesic grid by using spring dynamics. *J. Comput. Phys.*, **174**, 579–613, doi:10.1006/jcph.2001.6897.

——, M. Satoh, and K. Goto, 2002: An optimization of the icosahedral grid modified by spring dynamics. *J. Comput. Phys.*, **183**, 307–331, doi:10.1006/jcph.2002.7193.

Ullrich, P. A., and J. Guerra, 2015: Exploring the effects of a high-order vertical coordinate in a non-hydrostatic global model. *Proc. Comput. Sci.*, **51**, 2076–2085, doi:10.1016/j.procs.2015.05.475.

——, C. Jablonowski, J. Kent, P. H. Lauritzen, R. D. Nair, and M. A. Taylor, 2012: Dynamical Core Model Intercomparison Project (DCMIP) test case documents. DCMIP Summer School: July/30/2012–August/10/2012, 83 pp. [Available online at https://earthsystemcog.org/projects/dcmip/.]

Wang, H., J. J. Tribbia, F. Baer, A. Fournier, and M. Taylor, 2007: A spectral element version of CAM2. *Mon. Wea. Rev.*, **135**, 3825–3840, doi:10.1175/2007MWR2058.1.

Weller, H., 2014: Non-orthogonal version of the arbitrary polygonal C-grid and a new diamond grid. *Geosci. Model Dev.*, **7**, 779–797, doi:10.5194/gmd-7-779-2014.

——, J. Thuburn, and C. Cotter, 2012: Computational modes and grid imprinting on five quasi-uniform spherical C grids. *Mon. Wea. Rev.*, **140**, 2734–2755, doi:10.1175/MWR-D-11-00193.1.

Whitaker, J., 2015: HIWPP non-hydrostatic dynamical core tests: Results from idealized test cases. NOAA/ESRL/PSD, 28 pp. [Available online at https://www.weather.gov/media/sti/nggps/HIWPP_idealized_tests-v8%20revised%2005212015.pdf.]

Zhang, H., and M. Rančić, 2007: A global Eta model on quasi-uniform grids. *Quart. J. Roy. Meteor. Soc.*, **133**, 517–528, doi:10.1002/qj.17.